A helper NLR targets organellar membranes to trigger immunity

Tarhan Ibrahim[1†], Enoch Lok Him Yuen[1†], Hung-Yu Wang[1,2†], Freddie J. King[1†], AmirAli Toghani[3†], Jiorgos Kourelis[1†], Cristina Vuolo[1], Vanda Adamkova[1], Baptiste Castel[3], Jonathan D. G. Jones[3], Chih-Hang Wu[2], Sophien Kamoun[3]*, Tolga O. Bozkurt[1]*

Affiliations

[1] Department of Life Sciences, Imperial College London, London SW7 2AZ, UK.

[2] Institute of Plant and Microbial Biology, Academia Sinica, Taipei 115201 Taiwan.

[3] The Sainsbury Laboratory, University of East Anglia, Norwich Research Park, Norwich NR4 7UH, UK.

[†]These authors contributed equally to this work.

*Corresponding authors: o.bozkurt@imperial.ac.uk (TOB) and sophien.kamoun@tsl.ac.uk (S.K.)

Abstract

In plants, NLR (nucleotide-binding domain and leucine-rich repeat) proteins execute innate immunity through the formation of resistosomes that accumulate at the plasma membrane. However, the extent to which NLR resistosomes target other cellular membranes is unknown. Here, we show that the helper NLR NRG1 engages with multiple organellar membranes to trigger innate immunity. Compared to other helper NLRs, NRG1 and closely related RPW8-like NLRs (CC_R-NLRs) possess extended N-termini with distinctive sequence signatures, enabling their assembly into longer structures than canonical coiled coil NLR (CC-NLR) resistosomes. Activated NRG1 associates with single- and double-membrane organelles via its N-terminal RPW8-like domain. Our findings reveal that plant NLR resistosomes accumulate at a variety of cellular membrane sites to activate immunity.

Introduction

Innate immunity relies on the precise recognition of pathogens by nucleotide-binding leucine-rich repeat receptors (NLRs), which orchestrate defense-related programmed cell death known as the hypersensitive response (HR) (*1, 2*). In mammals, activated NLRs assemble into inflammasomes that direct Gasdermin oligomers to the plasma membrane, leading to pyroptotic cell death and pathogen clearance (*3-5*). Similarly, in plants, activated NLRs assemble into oligomeric inflammasome-like structures called resistosomes, which are believed to ultimately target the plasma membrane to trigger cell death and restrict pathogen invasion (*6-8*). Despite these advances, the extent to which NLR resistosomes can target other cellular membranes remains unclear.

NLRs can function as singletons, in pairs, or within complex networks, where sensor NLRs recognize pathogen effectors and helper NLRs execute the HR (*9*). These multidomain proteins typically consist of a divergent N-terminal domain, a central NB-ARC domain, and a C-terminal leucine-rich repeat (LRR) domain. Plant NLRs are grouped into four main subclasses based on their phylogeny and N-terminal domains: toll/interleukin-1 receptor (TIR) NLRs (TIR-NLRs), RPW8-like NLRs (CC_R-NLRs), coiled-coil (CC) NLRs (CC-NLRs) and the G10 NLRs (*10*). Typically, these N-terminal domains mediate downstream immune signaling following recognition of pathogen effectors (*11-14*).

Canonical models of NLR activation include the CC-NLRs ZAR1, Sr35 and helper NLRs called NRCs, which oligomerize into either pentameric or hexameric resistosomes (*8, 15-20*). However, another well-characterized pathway is the NRG1/ADR1 network, where the CC_R-NLRs NRG1 and ADR1 function as helpers, triggering immune signaling and cell death downstream of multiple TIR-type sensor NLRs (*21-23*). These CC_R-NLR helpers form oligomers involved in membrane pore formation and calcium channel activity, triggering cell death in a manner similar to CC-NLR resistosomes (*6*). Upon activation, CC-NLRs and CC_R-NLRs produce distinctive punctate structures, likely representing clusters of resistosomes, which can be observed through confocal microscopy using C-terminal fluorescent tags (*16, 17, 24*). To date, these NLR puncta have been visualized at the plasma membrane although a recent report localized an atypical NLR protein at the vacuole (*25*).

Although divergent in sequence and phylogeny, CC_R-NLRs and CC-NLRs share a structurally similar 4-helix bundle CC domain, resembling those found in the N-terminus of proteins, such as mixed lineage kinase domain-like (MLKL), Casitas B-lineage lymphoma (Cbl), heterokaryon incompatibility (HET), and the HeLo domain in fungi (*6, 26-28*). How does variability in the 4-helix CC domain affect function and cellular dynamics? We utilized live imaging of CC_R-NLR proteins in plant cells, along with AlphaFold3 (AF3) predictions of NLR oligomers, to test the hypothesis that activated CC_R-NLRs target distinct subcellular compartments (*29*).

Results

CC_R-NLRs have extended N-termini compared to canonical CC-NLRs

To test our idea, we focused on the very N-terminus of CC_R-NLRs. In canonical CC-NLRs, such as ZAR1, Sr35 and NRCs, the MADA motif in the N-terminal α1-helix is essential for

initiating cell death by forming a funnel-like pore that inserts into the plasma membrane (*8, 15, 30*). In contrast, CC_R-NLRs lack this motif and instead possess distinct N-terminal sequence patterns specific to the NRG1 and ADR1 sub-clades (Fig 1A, S1, Data S1 to S6).

Although structural data on activated CC_R-NLR resistosomes are lacking, AF3 can be used to predict NLR oligomer structures with high accuracy (*19*). AF3 predicted that CC_R-NLR resistosomes have significantly longer funnel-shaped CC regions compared to CC-NLRs, suggesting a different interaction with cellular membranes (Fig 1B, S2, Data S7). Notably, the NbNRG1 resistosome exhibited an extended funnel-shaped CC structure, 45 Å longer than CC-NLRs like ZAR1, Sr35, and NRC2, beyond to the thickness of a single membrane (*31, 32*)(Fig 1B). AF3 predictions of resting states also showed structural differences, with NbNRG1 featuring an extended fourth α-helix not seen in CC-NLRs (Fig S3).

Activated NbNRG1 targets chloroplasts

To test the extent to which the longer CC domain of CC_R-NLRs mediates differential membrane targeting, we examined the subcellular localization of NbNRG1 using C-terminal GFP fusions. Expression of full-length NbNRG1:GFP induces cell death in the model plant *Nicotiana benthamiana* (*N. benthamiana*), as previously reported (*33, 34*) (Fig. S4). To address this issue, we resorted to using a truncated NbNRG1 lacking the first 14 amino acids ($NbNRG1^{\Delta 14}$, Fig. 2A), an equivalent truncation to the one used previously for AtNRG1.1 (Data S8) (*6*). This $NbNRG1^{\Delta 14}$:GFP triggered delayed and weak cell death compared to full-length NbNRG1:GFP when it was co-expressed with the gene silencing suppressor P19 or further activated by the bacterial effector XopQ, making it suitable for cell biology studies (Fig S4). $NbNRG1^{\Delta 14}$:GFP displayed a prominent punctate distribution when co-expressed with XopQ or P19, with a subset of the puncta localizing to chloroplasts (Fig. 2B). Co-expression with a negative control (GUS) revealed $NbNRG1^{\Delta 14}$ resting state, marked by cytoplasmic distribution (33%, N=12 cells), similar to other helper NLRs (*24*). However, $NbNRG1^{\Delta 14}$ remained partially autoactive and showed significant punctate distribution, with puncta localizing to chloroplasts in 66% of the observed cells (N=12) (Fig. 2B, Fig. S5A). When further activated by XopQ, this punctate localization became even more pronounced (100%, N=11/11 cells), with a subset of puncta associated with chloroplasts (Fig. S5A).

We used a CTP1-RFP fusion protein to label the chloroplast stroma (*35*), revealing that $NbNRG1^{\Delta 14}$ puncta were peripherally distributed relative to CTP1-RFP, indicating that activated $NbNRG1^{\Delta 14}$ engages with the chloroplast envelope (Fig. 2C). We also validated live-cell imaging observations with purified chloroplasts, confirming the punctate distribution of $NbNRG1^{\Delta 14}$ (Fig. 2D). We expressed $NbNRG1^{\Delta 14}$ under the weaker Arabidopsis Act2 promoter (pAtAct2), which, unlike 35S::$NbNRG1^{\Delta 14}$ did not induce visible cell death symptoms (Fig. S5B). pAtAct2::$NbNRG1^{\Delta 14}$ showed a weak cytoplasmic signal (78%, N=18 cells), with only a few cells displaying detectable puncta, some associated with chloroplasts (N=4/18 cells, Fig. S5B).

We further corroborated these results using a fusion of the full-length NbNRG1 with the monomeric fluorescent protein mKOK (NbNRG1-mKOK), which produces a weaker cell death compared to NbNRG1:GFP (Fig. S5B). NbNRG1-mKOK showed a mixed localization pattern in the few surviving cells, with either cytoplasmic distribution (resting state) or punctate

structures, some of which localized to chloroplasts in *nrg1* knockout plants (Fig. S6A). This pattern remained similar in *nrg1/adr1* double knockouts co-expressed with XopQ or a GUS negative control (Fig. S6B). Notably, NbNRG1-mKOK displayed more prominent puncta in the presence of XopQ (75% of cells, 16/20 images) compared to the negative control (30% of cells, 6/20 images). Furthermore, activation by XopQ of NbNRG1 expressed under the weaker Act2 promoter and fused to a brighter fluorophore td8ox2StayGold (*36*) revealed a prominent punctate distribution, with some puncta associated with chloroplasts (Fig. S6C, movie S1). Overall, these independent findings indicate that activated NbNRG1 can localize at the chloroplast outer envelope in a robust and reproducible fashion.

NbNRG1 localizes at mitochondria and endoplasmic reticulum (ER) but not Golgi

NbNRG1 puncta did not exclusively target chloroplasts, indicating an association with other membrane interfaces (Fig. 2, B and C; Figs. S5 and S6). To explore this, we co-expressed NbNRG1$^{\Delta 14}$:GFP with various organelle markers tagged with RFP. NbNRG1$^{\Delta 14}$:GFP puncta localized with markers for the endoplasmic reticulum (ER) and mitochondria, but not with Golgi or plasma membrane, nor with the cytoplasmic RFP control (Fig. 3, A to F). These findings demonstrate that activated NbNRG1 can target single or double membrane organelles.

These unexpected localization patterns raised the question of whether organelle-targeting is specific to activated NbNRG1 or a broader feature of activated helper NLRs. To investigate this, we co-expressed organelle markers with NRC4, a CC-type helper NLR that belongs to the NRC-immune network (*37*). To monitor the activated state of NRC4 we used an autoactive NRC4 mutant (NRC4$^{L9E/D478V}$:GFP) that carries the MHD motif mutation (D478V) and an N-terminal mutation in the MADA α1-helix (L9E) (*24*). This mutant prevents HR cell death but preserves NRC4 oligomerization, puncta formation, and membrane targeting (*24*). Consistent with earlier work (*24*), NRC4$^{L9E/D478V}$:GFP produced puncta that localize at the plasma membrane, but not the ER, Golgi, chloroplasts, or mitochondria (Fig. S7). These results suggest that not all activated helper NLRs target organelles, underscoring the specificity of NbNRG1 localization pattern.

The CC$_R$-NLRs NbNRG1 and NbADR1 exhibit contrasting sub-cellular localizations

CC$_R$-NLRs are divided into two subfamilies: NRG1 and ADR1 (Fig. 1A, S1). We next assessed whether, like NbNRG1, NbADR1 can also target organelles. Similar to NbNRG1:GFP, NbADR1:GFP showed autoactivity when expressed in *N. benthamiana*, inducing a strong HR cell death response, making live-cell imaging challenging. However, an N-terminal truncation (NbADR1$^{\Delta 14}$:GFP) version, lacking the first 14 amino acids, did not trigger HR cell death (Fig. S8). Unlike the randomly scattered puncta throughout the cell observed with NbNRG1$^{\Delta 14}$:GFP, NbADR1$^{\Delta 14}$:GFP displayed a sharp peripheral punctate distribution suggestive of membrane rather than organelle localization (Fig. S9). Indeed, co-expression of NbADR1$^{\Delta 14}$:GFP with organelle and plasma membrane markers confirmed that it primarily produces puncta at the plasma membrane, with no signal detected at the organelles (Fig. S9). While further studies are needed to fully elucidate the localization dynamics of full-length NbADR1, these results indicate that truncated NbADR1$^{\Delta 14}$ and NbNRG1$^{\Delta 14}$ accumulate at distinct membrane interfaces, highlighting functional divergence within the CC$_R$-NLR family.

NbNRG1 CC_R domain governs membrane localization

Recent studies have shown that NbNRG1 interacts with SAG101b in its resting state (*33*). To further investigate the differential membrane targeting of NbADR1 and NbNRG1, we examined the contribution of their upstream signaling components, such as EDS1/PAD4 and EDS1/SAG101, to this process. The subcellular localization patterns of NbNRG1$^{\Delta 14}$:GFP and NbADR1$^{\Delta 14}$:GFP remained unchanged when expressed in the *N. benthamiana epss* mutant (which lacks EDS1, PAD4, SAG101a, and SAG101b) (*38*) compared to wildtype plants (Fig. S10). This suggests that the differential localization patterns of activated NbNRG1 and NbADR1 are not solely determined by their signaling components.

We then hypothesized that the N-terminal CC domains of CC_R-NLRs might dictate their differential membrane targeting. To test this, we generated NbNRG1 and NbADR1 chimeras by swapping their CC_R domains, excluding the first 14 amino acids to avoid autoactive HR cell death (Fig. 4A), and assessed their localization patterns using membrane and organelle markers (Fig 4B). The NRG1/ADR1 chimera ($CC^{ADR1\Delta 14}$-NRG1), which carried the CC_R domain of NbADR1 fused to the NB-ARC and LRR domains of NbNRG1, exhibited plasma membrane rather than organelle localization, behaving similarly to NbADR1$^{\Delta 14}$. Conversely, the reciprocal chimera ($CC^{NRG1\Delta 14}$-ADR1), which carried the CC_R domain of NbNRG1 fused to NB-ARC and LRR domains of NbADR1, produced puncta that localized to organelles but not to the plasma membrane, mimicking the behavior of NbNRG1$^{\Delta 14}$ (Fig. 4B)

Moreover, swapping the CC_R domains also resulted in a switch in the cell death activity of the CC_R-NLRs (Fig. 4C). The $CC^{ADR1\Delta 14}$-NRG1 chimera, carrying the CC_R domain of NbADR1, lost its ability to trigger HR, while the $CC^{NRG1\Delta 14}$-ADR1 chimera, carrying the CC_R domain of NbNRG1, gained the ability to activate cell death (Fig. 4C). These findings indicate that the CC_R domains of NbNRG1 and NbADR1 are crucial in determining both their differential membrane targeting and HR activation capacities. Altogether, these findings lead us to propose that activated helper NLRs can associate with different membrane interfaces, targeting plasma membrane or organelles to trigger immunity and disease resistance (Fig. 4D).

Discussion

CC_R-NLRs function as an ancient class of helper NLRs widely conserved across land plant lineages, where they are essential for executing TIR-NLR driven immunity (*27*). Here, we reveal that an activated CC_R-NLR, NbNRG1, exhibits distinct membrane localization patterns by localizing to various organelles (Fig. 1, 2, and 3). This sharply contrasts with the plasma membrane-targeting activity of canonical CC-NLRs, suggesting a unique mechanism for cell death activation beyond plasma membrane pore formation and cation channel activity (*8, 24*).

The N-terminal diversity of CC-NLR immune proteins is stunning despite the overall conservation of the four-helix bundle structure of the CC domain (*6*). However, the biological functions and drivers of this extreme diversification of the N-terminal CC domain remain poorly understood. The structural model of the NRG1 resistosome predicts an extended N-terminal funnel-shaped structure—a unique feature of these CC_R-NLR proteins that would enable them to span across double membrane organelles, such as those of chloroplasts and mitochondria (Fig. 1B). This structural adaptation may underpin the robustness of NRG1 immune activation capabilities across a diverse range of plant tissues and species (*23*).

Although both NRG1 and ADR1 are CC_R-NLRs activated by upstream TIR-NLRs (*39*), our findings indicate they target different membranes. Consistent with this, Arabidopsis NRG1 and ADR1 have been shown to elicit different immune responses. NRG1 is associated with cell death responses (*23*), whereas ADR1 is implicated in transcriptional reprogramming in Arabidopsis (*40*), suggesting distinct modes of action to execute immunity. In agreement with this notion, swapping the CC_R domains between NbNRG1 and NbADR1 led to shifts in both localization and cell death (Fig. 4), underscoring the key role of the CC_R domain in determining membrane specificity of CC_R-NLR resistosomes.

The ability of NRG1 to target calcium-rich organelles such as chloroplasts, mitochondria, and the ER may enable it to tap into alternative intracellular calcium stores, to amplify the cell death immune response (*41*). By diversifying its subcellular localization, NRG1 may have evolved to initiate immune responses via multiple membrane interfaces. This may present a multi-compartmental defense strategy to counteract pathogen effectors that suppress activated NLR functions at the plasma membrane, and therefore sustain robust immunity.

NRG1 organelle localization supports a model in which NLR-mediated innate immune signaling is more compartmentalized and complex than anticipated. Our findings align with recent research emphasizing the critical role of chloroplasts in immunity (*42, 43*). Upon immune activation, chloroplasts downregulate photosynthesis and produce reactive oxygen species (ROS), defense hormones, and facilitate signaling through the MAPK pathway (*44-48*), processes that are tightly linked to NLR-mediated immunity. NRG1 may tap into these physiological processes, further linking organellar function to NLR-triggered immunity.

Overall, our findings highlight the critical role of the NLR resistosome architecture in enabling distinct membrane targeting and consequent immune responses. These insights also offer new opportunities for NLR bioengineering, paving the way for developing enhanced plant immunity by exploiting the flexibility of NLR molecular systems to engage multiple membrane interfaces.

Acknowledgements

We thank the Imperial College FILM facility for their technical expertise and provision of our microscopy equipment.

Funding

Biotechnology and Biological Sciences Research Council (BBSRC) Impact Acceleration Fund BB/X511055/1 (T.I.)

BBSRC BB/X016382/1 (E.L.H.Y. and T.O.B.)

National Science and Technology Council NSTC-112-2628-B-001-007, NSTC 113-2927-I-001-514 (H.Y.W. and C.H.W.)

The Gatsby Charitable foundation (A.T., S.K., B.C. and J.D.G.J.)

BBSRC BB/P012574 (Plant Health ISP) (A.T. and S.K.)

BBSRC BBS/E/J/000PR9795 (A.T. and S.K.)

BBSRC BBS/E/J/000PR9796 (Plant Health ISP – Response) (A.T. and S.K.)

BBSRC BBS/E/J/000PR9797 (Plant Health ISP – Susceptibility) (A.T. and S.K.)

BBSRC BBS/E/J/000PR9798 (Plant Health ISP – Evolution) (A.T. and S.K.)

BBSRC BB/V002937/1 (A.T. and S.K.)

UK Research and Innovation (UKRI) EP/Y032187/1 (A.T. and S.K.)

European Research Council (ERC) BLASTOFF 743165 (A.T. and S.K.)

Author contributions

Conceptualization: T.I., E.L.H.Y., H.W.Y., F.J.K., A.T., J.K., T.O.B.

Methodology: T.I., E.L.H.Y., H.W.Y., F.J.K., A.T., J.K., T.O.B.

Investigation: T.I., E.L.H.Y., H.W.Y., F.J.K., A.T., J.K., C.V., V.A., B.C., T.O.B.

Visualisation: T.I., E.L.H.Y., A.T., T.O.B.

Funding acquisition: T.O.B., C.H.W., S.K., J.D.G.J.

Project administration: T.I., E.L.H.Y., H.W.Y., F.J.K., A.T., J.K., T.O.B.

Supervision: T.O.B., C.H.W., S.K., J.D.G.J.

Writing – original draft: T.I., E.L.H.Y., S.K., T.O.B

Writing – review & editing: T.I., E.L.H.Y., H.W.Y., F.J.K., A.T., J.K., S.K., J.D.G.J., C.H.W., T.O.B.

Competing interests

T.O.B. and S.K. receive funding from industry and co-founded a start-up company (Resurrect Bio Ltd.) on NLR biology. S.K. filed patents on NLR biology.

Supplementary Materials

Materials and Methods

Figs S1 to S10

Movie S1

Data S1 to S10

Fig. 1. RPW8-like NLRs exhibit distinct phylogenetic and structural characteristics in their coiled-coil domains. (A) The phylogenetic tree illustrates the relationships among 1,149 RPW8-like (CC_R) NLRs based on their NB-ARC domain sequences. Two well-supported clades are highlighted: the ADR1 clade (red) with 359 sequences and the NRG1 clade (blue) with 769 sequences. Distinct N-terminal motifs in the RPW8-like CC domains of each clade were identified using MEME analysis. The tree is rooted with sequences from AtZAR1, NbZAR1, and NRCs from tomato as the outgroup. **(B)** AlphaFold3 predicted coiled-coil domain models of AtZAR1, TmSr35, NbNRC2, NbADR1 and NbNRG1. Structures are coloured by pLDDT values. NRG1 and ADR1 were modeled as pentamers as we observed higher pTM and ipTM scores compared to hexamers. AlphaFold3 models and their confidence analysis can be found at Data S7 and Fig. S2, respectively.

Fig. 2. Activated NbNRG1 targets the outer chloroplast membrane. (A) AlphaFold3 predicted resistosome structures for full-length NRG1 and NRG1 with the first 14 amino acids truncated. NbNRG1 resistosomes are coloured in pink. **(B)** Confocal micrograph of *N. benthamiana* leaf epidermal cells transiently expressing NbNRG1$^{\Delta 14}$:GFP with XopQ, P19 or GUS. Images shown are single-plane images. Dashed lines in overlay panels correspond to inset. Scale bars represent 10 µm. **(C)** Confocal micrograph of *N. benthamiana* leaf epidermal cells transiently expressing NbNRG1$^{\Delta 14}$:GFP with XopQ and CTP1-RFP to mark the stroma. Images shown are single-plane images. Dashed lines in the overlay panel correspond to line intensity plots depicting the relative fluorescence across the marked area. Scale bars represent 10 µm. **(D)** Confocal micrograph of purified chloroplasts (CPs) from *N. benthamiana* leaf epidermal cells transiently expressing NbNRG1$^{\Delta 14}$:GFP with P19. Dashed line in the overlay panel corresponds to a line intensity plot depicting the relative fluorescence across the marked area. Scale bars represent 10 µm.

Fig. 3. NbNRG1 can target the endoplasmic reticulum and mitochondria but does not localize to the Golgi or plasma membrane. (A) Confocal micrograph of *N. benthamiana* leaf epidermal cells transiently expressing NbNRG1$^{\Delta 14}$:GFP with SP:RFP:HDEL. Images shown

are single-plane images. Dashed lines in overlay panels correspond to color inverted inset. Scale bars represent 10 µm. **(B)** Confocal micrograph of *N. benthamiana* leaf epidermal cells transiently expressing NbNRG1$^{\Delta 14}$:GFP with ScCOX41-29:mCherry. Images shown are single-plane images. Dashed lines in overlay panels correspond to inset. Scale bars represent 10 µm. **(C)** Confocal micrograph of *N. benthamiana* leaf epidermal cells transiently expressing NbNRG1$^{\Delta 14}$:GFP with GmMan11-49:mCherry. Images shown are single-plane images. Dashed lines in overlay panels correspond to inset. Scale bars represent 10 µm. **(D)** Confocal micrograph of *N. benthamiana* leaf epidermal cells transiently expressing NbNRG1$^{\Delta 14}$:GFP with RFP:Remorin1.3. Images shown are single-plane images. Dashed lines in overlay panels correspond to inset. Scale bars represent 10 µm. **(E)** Confocal micrograph of *N. benthamiana* leaf epidermal cells transiently expressing NbNRG1$^{\Delta 14}$:GFP with RFP:EV. Images shown are single-plane images. Dashed lines in overlay panels correspond to inset. Scale bars represent 10 µm.

Fig. 4. NbNRG1 coiled-coil domain dictates cellular localization. (A) AlphaFold3 predicted structures for CC$^{ADR1\Delta 14}$-NB-ARC-LRR-NRG1 and CC$^{NRG1\Delta 14}$-NB-ARC-LRR-ADR1 CC domain swap resistosomes. Domains originating from NRG1 and ADR1 are coloured pink and blue, respectively. **(B)** Confocal micrographs of *N. benthamiana* leaf epidermal cells transiently expressing CC$^{ADR1\Delta 14}$-NB-ARC-LRR-NRG1:GFP (left panels) or CC$^{NRG1\Delta 14}$-NB-ARC-LRR-ADR1:GFP (right panels) with CTP1-RFP (chloroplast), RFP-Remorin1.3 (plasma membrane), SP:RFP:HDEL (ER) or RFP:EV (control). Images shown are single-plane images. Dashed lines in merged panels correspond to inset. Scale bars represent 10 µm. **(C)** A representative leaf picture from *N. benthamiana nrg1/adr1* double KO plants showing HR after expression of ADR1$^{\Delta 14}$:GFP, NRG1$^{\Delta 14}$:GFP, CC$^{ADR1\Delta 14}$-NRG1:GFP or CC$^{NRG1\Delta 14}$-ADR1:GFP. Box and dot plot showing the normalized HR signal at 800 nm (infrared) for 15 leaves. Each leaf is highlighted with a green dot and the mean value for that condition in a larger pink dot. Raw and normalized HR intensity values can be found at Data S10. **(D)** A representative model for differential NLR localization upon pathogen recognition. NRC4 targets the plasma membrane, whereas NRG1 can target various intracellular membrane compartments.

Fig. 1

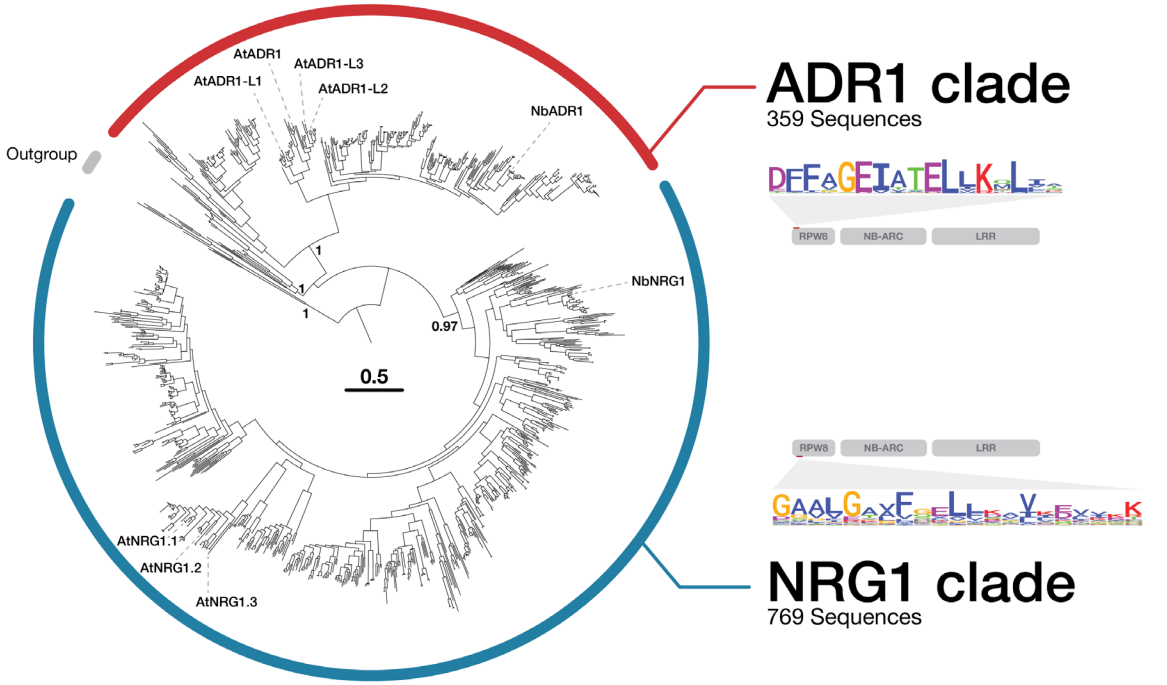
A
AtADR1
AtADR1-L3
AtADR1-L1
AtADR1-L2
NbADR1
Outgroup
1
1
1
NbNRG1
0.97
0.5
AtNRG1.1
AtNRG1.2
AtNRG1.3
ADR1 clade
359 Sequences
RPW8
NB-ARC
LRR
RPW8
NB-ARC
LRR
NRG1 clade
769 Sequences

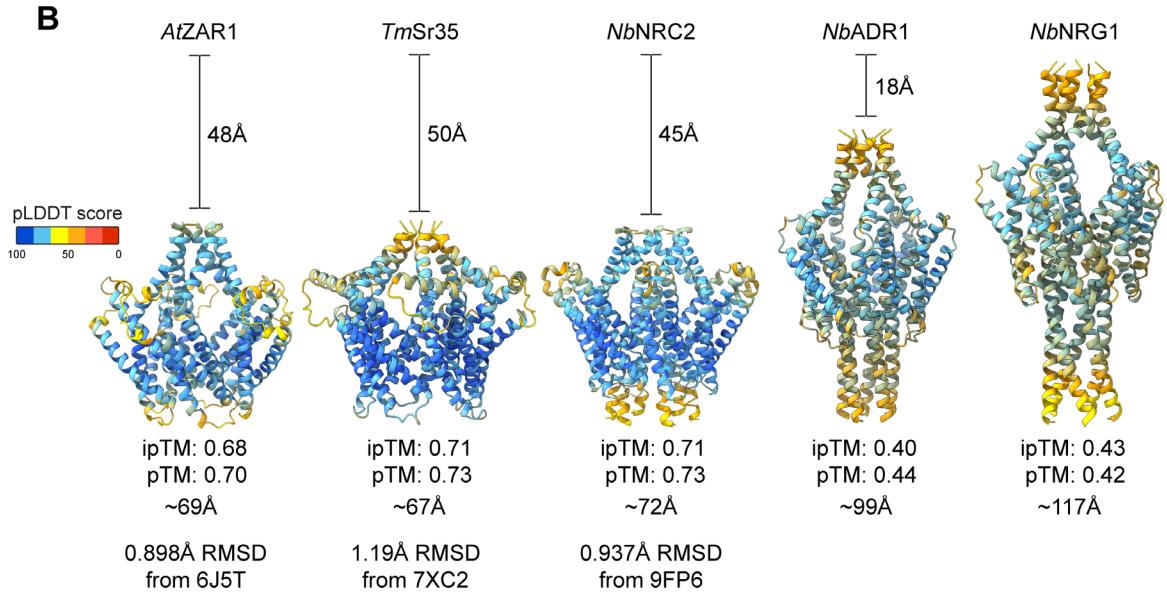
B
AtZAR1
TmSr35
NbNRC2
NbADR1
NbNRG1
48Å
50Å
45Å
18Å
pLDDT score
100
50
0
ipTM: 0.68
pTM: 0.70
~69Å
0.898Å RMSD
from 6J5T
ipTM: 0.71
pTM: 0.73
~67Å
1.19Å RMSD
from 7XC2
ipTM: 0.71
pTM: 0.73
~72Å
0.937Å RMSD
from 9FP6
ipTM: 0.40
pTM: 0.44
~99Å
ipTM: 0.43
pTM: 0.42
~117Å

Fig. 2

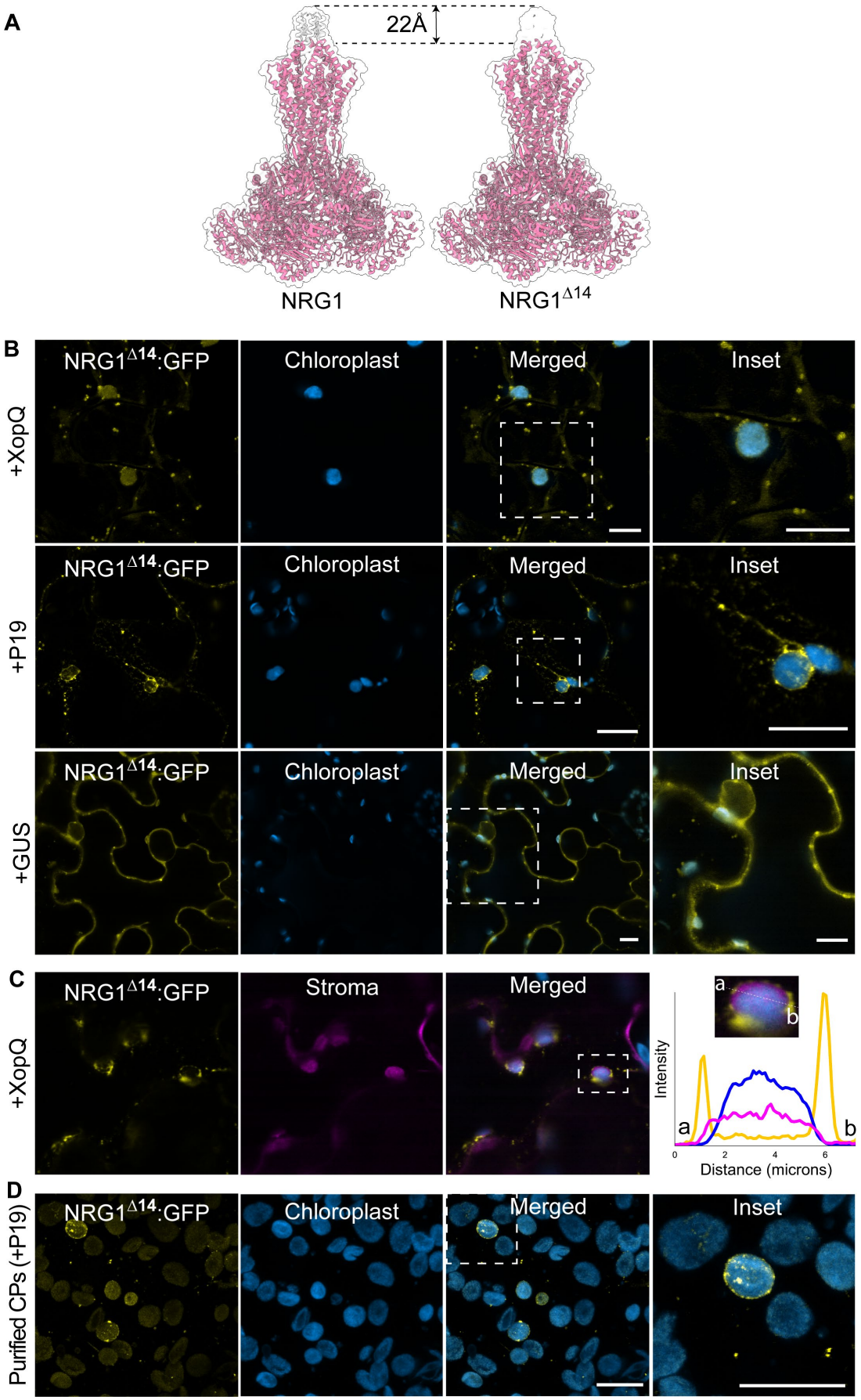
A
22Å
NRG1
NRG1Δ14
B
+XopQ
+P19
+GUS
NRG1Δ14:GFP
Chloroplast
Merged
Inset
C
+XopQ
NRG1Δ14:GFP
Stroma
Merged
a
b
Intensity
Distance (microns)
0
2
4
6
D
Purified CPs (+P19)
NRG1Δ14:GFP
Chloroplast
Merged
Inset

Fig. 3

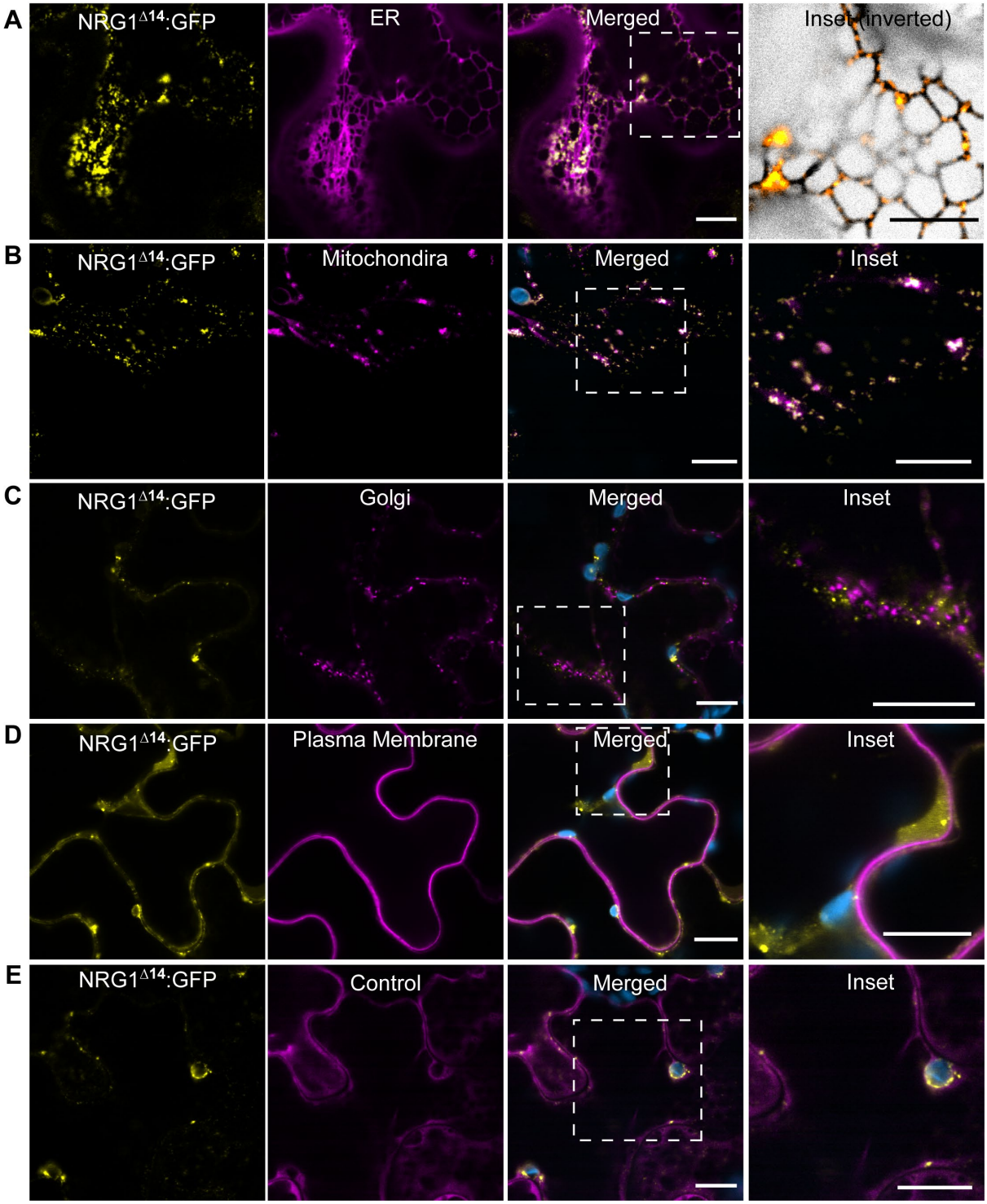
A
NRG1Δ14:GFP
ER
Merged
Inset (inverted)
B
NRG1Δ14:GFP
Mitochondira
Merged
Inset
C
NRG1Δ14:GFP
Golgi
Merged
Inset
D
NRG1Δ14:GFP
Plasma Membrane
Merged
Inset
E
NRG1Δ14:GFP
Control
Merged
Inset

Fig. 4

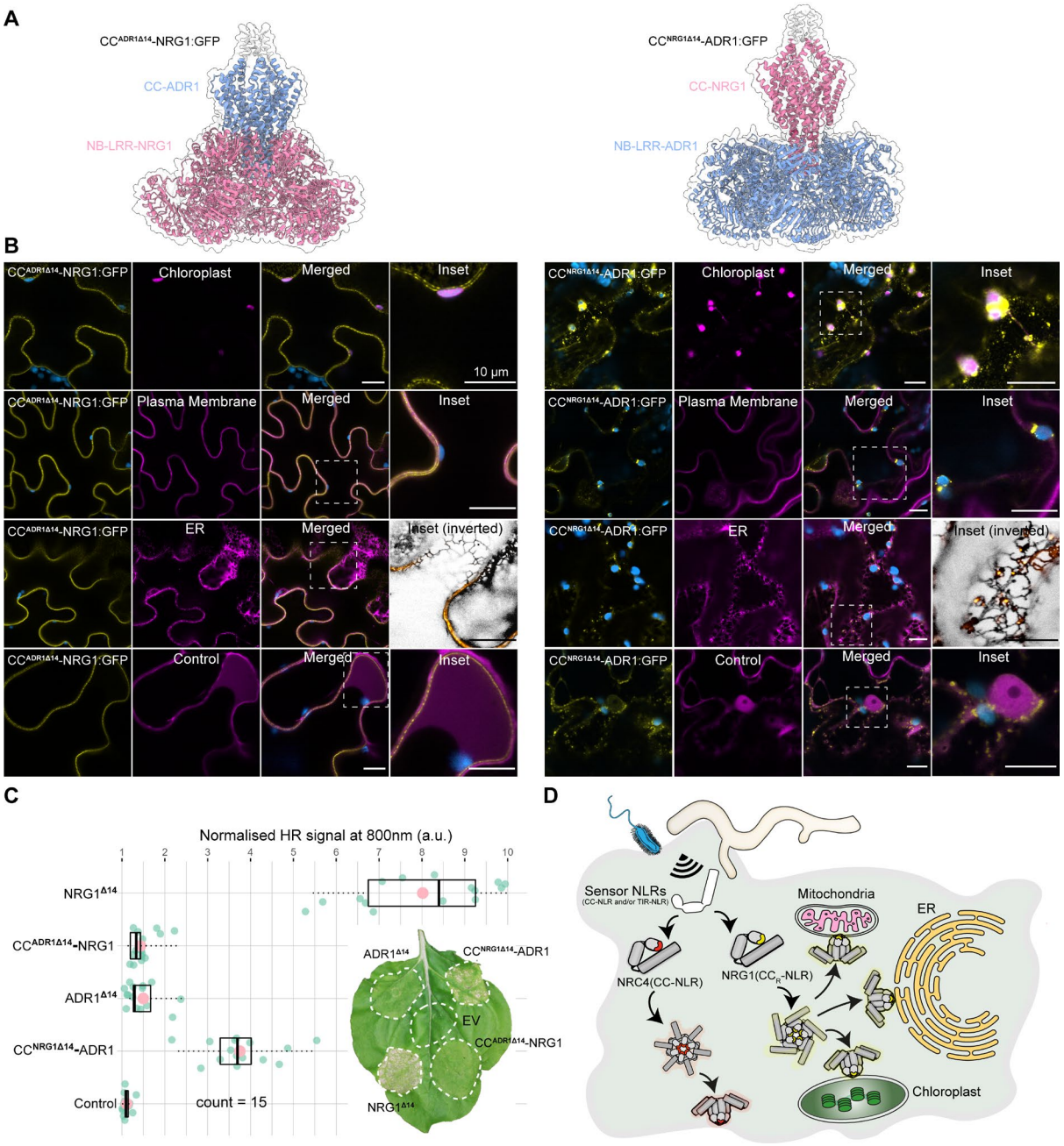
A
CC^ADR1Δ14-NRG1:GFP
CC-ADR1
NB-LRR-NRG1
CC^NRG1Δ14-ADR1:GFP
CC-NRG1
NB-LRR-ADR1
B
CC^ADR1Δ14-NRG1:GFP
Chloroplast
Merged
Inset
10 µm
Plasma Membrane
ER
Inset (inverted)
Control
CC^NRG1Δ14-ADR1:GFP
C
Normalised HR signal at 800nm (a.u.)
NRG1^Δ14
CC^ADR1Δ14-NRG1
ADR1^Δ14
CC^NRG1Δ14-ADR1
Control
count = 15
EV
D
Sensor NLRs
(CC-NLR and/or TIR-NLR)
Mitochondria
ER
NRC4(CC-NLR)
NRG1(CC_R-NLR)
Chloroplast

References

1. Z. Duxbury, C. H. Wu, P. Ding, A Comparative Overview of the Intracellular Guardians of Plants and Animals: NLRs in Innate Immunity and Beyond. *Annu Rev Plant Biol* **72**, 155-184 (2021).
2. B. Sundaram, R. E. Tweedell, S. Prasanth Kumar, T. D. Kanneganti, The NLR family of innate immune and cell death sensors. *Immunity* **57**, 674-699 (2024).
3. C. L. Evavold, I. Hafner-Bratkovic, P. Devant, J. M. D'Andrea, E. M. Ngwa, E. Borsic, J. G. Doench, M. W. LaFleur, A. H. Sharpe, J. R. Thiagarajah, J. C. Kagan, Control of gasdermin D oligomerization and pyroptosis by the Ragulator-Rag-mTORC1 pathway. *Cell* **184**, 4495-4511 e4419 (2021).
4. N. Kayagaki, I. B. Stowe, B. L. Lee, K. O'Rourke, K. Anderson, S. Warming, T. Cuellar, B. Haley, M. Roose-Girma, Q. T. Phung, P. S. Liu, J. R. Lill, H. Li, J. Wu, S. Kummerfeld, J. Zhang, W. P. Lee, S. J. Snipas, G. S. Salvesen, L. X. Morris, L. Fitzgerald, Y. Zhang, E. M. Bertram, C. C. Goodnow, V. M. Dixit, Caspase-11 cleaves gasdermin D for non-canonical inflammasome signalling. *Nature* **526**, 666-671 (2015).
5. B. Sundaram, N. Pandian, R. Mall, Y. Wang, R. Sarkar, H. J. Kim, R. K. S. Malireddi, R. Karki, L. J. Janke, P. Vogel, T. D. Kanneganti, NLRP12-PANoptosome activates PANoptosis and pathology in response to heme and PAMPs. *Cell* **186**, 2783-2801 e2720 (2023).
6. P. Jacob, N. H. Kim, F. Wu, F. El-Kasmi, Y. Chi, W. G. Walton, O. J. Furzer, A. D. Lietzan, S. Sunil, K. Kempthorn, M. R. Redinbo, Z. M. Pei, L. Wan, J. L. Dangl, Plant "helper" immune receptors are Ca(2+)-permeable nonselective cation channels. *Science* **373**, 420-425 (2021).
7. J. Wang, M. Hu, J. Wang, J. Qi, Z. Han, G. Wang, Y. Qi, H. W. Wang, J. M. Zhou, J. Chai, Reconstitution and structure of a plant NLR resistosome conferring immunity. *Science* **364**, (2019).
8. G. Bi, M. Su, N. Li, Y. Liang, S. Dang, J. Xu, M. Hu, J. Wang, M. Zou, Y. Deng, Q. Li, S. Huang, J. Li, J. Chai, K. He, Y. H. Chen, J. M. Zhou, The ZAR1 resistosome is a calcium-permeable channel triggering plant immune signaling. *Cell* **184**, 3528-3541 e3512 (2021).
9. H. Adachi, L. Derevnina, S. Kamoun, NLR singletons, pairs, and networks: evolution, assembly, and regulation of the intracellular immunoreceptor circuitry of plants. *Curr Opin Plant Biol* **50**, 121-131 (2019).
10. J. Kourelis, T. Sakai, H. Adachi, S. Kamoun, RefPlantNLR is a comprehensive collection of experimentally validated plant disease resistance proteins from the NLR family. *PLoS Biol* **19**, e3001124 (2021).
11. K. S. Chia, P. Carella, Taking the lead: NLR immune receptor N-terminal domains execute plant immune responses. *New Phytol* **240**, 496-501 (2023).
12. M. P. Contreras, D. Ludke, H. Pai, A. Toghani, S. Kamoun, NLR receptors in plant immunity: making sense of the alphabet soup. *EMBO Rep* **24**, e57495 (2023).
13. S. Shepherd, E. L. H. Yuen, P. Carella, T. O. Bozkurt, The wheels of destruction: Plant NLR immune receptors are mobile and structurally dynamic disease resistance proteins. *Curr Opin Plant Biol* **74**, 102372 (2023).
14. E. L. H. Yuen, S. Shepherd, T. O. Bozkurt, Traffic Control: Subversion of Plant Membrane Trafficking by Pathogens. *Annu Rev Phytopathol* **61**, 325-350 (2023).
15. A. Forderer, E. Li, A. W. Lawson, Y. N. Deng, Y. Sun, E. Logemann, X. Zhang, J. Wen, Z. Han, J. Chang, Y. Chen, P. Schulze-Lefert, J. Chai, A wheat resistosome

defines common principles of immune receptor channels. *Nature* **610**, 532-539 (2022).
16. M. P. Contreras, H. Pai, M. Selvaraj, A. Toghani, D. M. Lawson, Y. Tumtas, C. Duggan, E. L. H. Yuen, C. E. M. Stevenson, A. Harant, A. Maqbool, C. H. Wu, T. O. Bozkurt, S. Kamoun, L. Derevnina, Resurrection of plant disease resistance proteins via helper NLR bioengineering. *Sci Adv* **9**, eadg3861 (2023).
17. M. P. Contreras, H. Pai, Y. Tumtas, C. Duggan, E. L. H. Yuen, A. V. Cruces, J. Kourelis, H. K. Ahn, K. T. Lee, C. H. Wu, T. O. Bozkurt, L. Derevnina, S. Kamoun, Sensor NLR immune proteins activate oligomerization of their NRC helpers in response to plant pathogens. *EMBO J* **42**, e111519 (2023).
18. F. Liu, Z. Yang, C. Wang, Z. You, R. Martin, W. Qiao, J. Huang, P. Jacob, J. L. Dangl, J. E. Carette, S. Luan, E. Nogales, B. J. Staskawicz, Activation of the helper NRC4 immune receptor forms a hexameric resistosome. *Cell*, (2024).
19. J. Madhuprakash, A. Toghani, M. P. Contreras, A. Posbeyikian, J. Richardson, J. Kourelis, T. O. Bozkurt, M. Webster, S. Kamoun, A disease resistance protein triggers oligomerization of its NLR helper into a hexameric resistosome to mediate innate immunity. *bioRxiv*, 2024.2006.2018.599586 (2024).
20. M. Selvaraj, A. Toghani, H. Pai, Y. Sugihara, J. Kourelis, E. L. H. Yuen, T. Ibrahim, H. Zhao, R. Xie, A. Maqbool, J. C. D. l. Concepcion, M. J. Banfield, L. Derevnina, B. Petre, D. M. Lawson, T. O. Bozkurt, C.-H. Wu, S. Kamoun, M. P. Contreras, Activation of plant immunity through conversion of a helper NLR homodimer into a resistosome. *bioRxiv*, 2023.2012.2017.572070 (2023).
21. S. Ma, D. Lapin, L. Liu, Y. Sun, W. Song, X. Zhang, E. Logemann, D. Yu, J. Wang, J. Jirschitzka, Z. Han, P. Schulze-Lefert, J. E. Parker, J. Chai, Direct pathogen-induced assembly of an NLR immune receptor complex to form a holoenzyme. *Science* **370**, (2020).
22. R. Martin, T. Qi, H. Zhang, F. Liu, M. King, C. Toth, E. Nogales, B. J. Staskawicz, Structure of the activated ROQ1 resistosome directly recognizing the pathogen effector XopQ. *Science* **370**, (2020).
23. B. Castel, P. M. Ngou, V. Cevik, A. Redkar, D. S. Kim, Y. Yang, P. Ding, J. D. G. Jones, Diverse NLR immune receptors activate defence via the RPW8-NLR NRG1. *New Phytol* **222**, 966-980 (2019).
24. C. Duggan, E. Moratto, Z. Savage, E. Hamilton, H. Adachi, C. H. Wu, A. Y. Leary, Y. Tumtas, S. M. Rothery, A. Maqbool, S. Nohut, T. R. Martin, S. Kamoun, T. O. Bozkurt, Dynamic localization of a helper NLR at the plant-pathogen interface underpins pathogen recognition. *Proc Natl Acad Sci U S A* **118**, (2021).
25. S. Sunil, S. Beeh, E. Stobbe, K. Fischer, F. Wilhelm, A. Meral, C. Paris, L. Teasdale, Z. Jiang, L. Zhang, M. Urban, E. Aguilar Parras, T. Nurnberger, D. Weigel, R. Lozano-Duran, F. El Kasmi, Activation of an atypical plant NLR with an N-terminal deletion initiates cell death at the vacuole. *EMBO Rep*, (2024).
26. A. R. Bentham, R. Zdrzalek, J. C. De la Concepcion, M. J. Banfield, Uncoiling CNLs: Structure/Function Approaches to Understanding CC Domain Function in Plant NLRs. *Plant Cell Physiol* **59**, 2398-2408 (2018).
27. K. S. Chia, J. Kourelis, A. Teulet, M. Vickers, T. Sakai, J. F. Walker, S. Schornack, S. Kamoun, P. Carella, The N-terminal domains of NLR immune receptors exhibit structural and functional similarities across divergent plant lineages. *Plant Cell* **36**, 2491-2511 (2024).
28. A. Daskalov, B. Habenstein, R. Sabate, M. Berbon, D. Martinez, S. Chaignepain, B. Coulary-Salin, K. Hofmann, A. Loquet, S. J. Saupe, Identification of a novel cell

death-inducing domain reveals that fungal amyloid-controlled programmed cell death is related to necroptosis. *Proc Natl Acad Sci U S A* **113**, 2720-2725 (2016).
29. J. Abramson, J. Adler, J. Dunger, R. Evans, T. Green, A. Pritzel, O. Ronneberger, L. Willmore, A. J. Ballard, J. Bambrick, S. W. Bodenstein, D. A. Evans, C. C. Hung, M. O'Neill, D. Reiman, K. Tunyasuvunakool, Z. Wu, A. Zemgulyte, E. Arvaniti, C. Beattie, O. Bertolli, A. Bridgland, A. Cherepanov, M. Congreve, A. I. Cowen-Rivers, A. Cowie, M. Figurnov, F. B. Fuchs, H. Gladman, R. Jain, Y. A. Khan, C. M. R. Low, K. Perlin, A. Potapenko, P. Savy, S. Singh, A. Stecula, A. Thillaisundaram, C. Tong, S. Yakneen, E. D. Zhong, M. Zielinski, A. Zidek, V. Bapst, P. Kohli, M. Jaderberg, D. Hassabis, J. M. Jumper, Accurate structure prediction of biomolecular interactions with AlphaFold 3. *Nature* **630**, 493-500 (2024).
30. H. Adachi, M. P. Contreras, A. Harant, C. H. Wu, L. Derevnina, T. Sakai, C. Duggan, E. Moratto, T. O. Bozkurt, A. Maqbool, J. Win, S. Kamoun, An N-terminal motif in NLR immune receptors is functionally conserved across distantly related plant species. *Elife* **8**, (2019).
31. B. Daum, D. Nicastro, J. Austin, 2nd, J. R. McIntosh, W. Kuhlbrandt, Arrangement of photosystem II and ATP synthase in chloroplast membranes of spinach and pea. *Plant Cell* **22**, 1299-1312 (2010).
32. M. S. Sommer, B. Daum, L. E. Gross, B. L. Weis, O. Mirus, L. Abram, U. G. Maier, W. Kuhlbrandt, E. Schleiff, Chloroplast Omp85 proteins change orientation during evolution. *Proc Natl Acad Sci U S A* **108**, 13841-13846 (2011).
33. J. Chen, X. Zhang, M. Bernoux, J. P. Rathjen, P. N. Dodds, Plant Toll/interleukin-1 receptor/resistance protein domains physically associate with enhanced disease susceptibility1 family proteins in immune signaling. *iScience* **27**, 108817 (2024).
34. D. Silhavy, A. Molnar, A. Lucioli, G. Szittya, C. Hornyik, M. Tavazza, J. Burgyan, A viral protein suppresses RNA silencing and binds silencing-generated, 21- to 25-nucleotide double-stranded RNAs. *EMBO J* **21**, 3070-3080 (2002).
35. B. Petre, C. Lorrain, D. G. Saunders, J. Win, J. Sklenar, S. Duplessis, S. Kamoun, Rust fungal effectors mimic host transit peptides to translocate into chloroplasts. *Cell Microbiol* **18**, 453-465 (2016).
36. R. Ando, S. Shimozono, H. Ago, M. Takagi, M. Sugiyama, H. Kurokawa, M. Hirano, Y. Niino, G. Ueno, F. Ishidate, T. Fujiwara, Y. Okada, M. Yamamoto, A. Miyawaki, StayGold variants for molecular fusion and membrane-targeting applications. *Nat Methods* **21**, 648-656 (2024).
37. C. H. Wu, A. Abd-El-Haliem, T. O. Bozkurt, K. Belhaj, R. Terauchi, J. H. Vossen, S. Kamoun, NLR network mediates immunity to diverse plant pathogens. *Proc Natl Acad Sci U S A* **114**, 8113-8118 (2017).
38. D. Lapin, V. Kovacova, X. Sun, J. A. Dongus, D. Bhandari, P. von Born, J. Bautor, N. Guarneri, J. Rzemieniewski, J. Stuttmann, A. Beyer, J. E. Parker, A Coevolved EDS1-SAG101-NRG1 Module Mediates Cell Death Signaling by TIR-Domain Immune Receptors. *Plant Cell* **31**, 2430-2455 (2019).
39. X. Sun, D. Lapin, J. M. Feehan, S. C. Stolze, K. Kramer, J. A. Dongus, J. Rzemieniewski, S. Blanvillain-Baufume, A. Harzen, J. Bautor, P. Derbyshire, F. L. H. Menke, I. Finkemeier, H. Nakagami, J. D. G. Jones, J. E. Parker, Pathogen effector recognition-dependent association of NRG1 with EDS1 and SAG101 in TNL receptor immunity. *Nat Commun* **12**, 3335 (2021).
40. S. C. Saile, P. Jacob, B. Castel, L. M. Jubic, I. Salas-Gonzales, M. Backer, J. D. G. Jones, J. L. Dangl, F. El Kasmi, Two unequally redundant "helper" immune receptor families mediate Arabidopsis thaliana intracellular "sensor" immune receptor functions. *PLoS Biol* **18**, e3000783 (2020).

41. S. Stael, B. Wurzinger, A. Mair, N. Mehlmer, U. C. Vothknecht, M. Teige, Plant organellar calcium signalling: an emerging field. *J Exp Bot* **63**, 1525-1542 (2012).
42. P. Kachroo, T. M. Burch-Smith, M. Grant, An Emerging Role for Chloroplasts in Disease and Defense. *Annu Rev Phytopathol* **59**, 423-445 (2021).
43. E. L. H. Yuen, Z. Savage, V. Adamkova, C. Vuolo, Y. Zhou, Y. Tumtas, J. L. Erickson, J. Prautsch, A. I. Balmez, J. Stuttmann, C. Duggan, F. Rivetti, C. Molinari, M. Schattat, T. O. Bozkurt, Membrane Contact Sites Between Chloroplasts and Pathogen Interface Underpin Plant Focal Immune Responses. *bioRxiv*, 2021.2010.2008.463641 (2024).
44. M. de Torres Zabala, G. Littlejohn, S. Jayaraman, D. Studholme, T. Bailey, T. Lawson, M. Tillich, D. Licht, B. Bolter, L. Delfino, W. Truman, J. Mansfield, N. Smirnoff, M. Grant, Chloroplasts play a central role in plant defence and are targeted by pathogen effectors. *Nat Plants* **1**, 15074 (2015).
45. C. Gao, H. Xu, J. Huang, B. Sun, F. Zhang, Z. Savage, C. Duggan, T. Yan, C. H. Wu, Y. Wang, V. Vleeshouwers, S. Kamoun, T. O. Bozkurt, S. Dong, Pathogen manipulation of chloroplast function triggers a light-dependent immune recognition. *Proc Natl Acad Sci U S A* **117**, 9613-9620 (2020).
46. J. Jelenska, N. Yao, B. A. Vinatzer, C. M. Wright, J. L. Brodsky, J. T. Greenberg, A J domain virulence effector of Pseudomonas syringae remodels host chloroplasts and suppresses defenses. *Curr Biol* **17**, 499-508 (2007).
47. Q. Xu, C. Tang, X. Wang, S. Sun, J. Zhao, Z. Kang, X. Wang, An effector protein of the wheat stripe rust fungus targets chloroplasts and suppresses chloroplast function. *Nat Commun* **10**, 5571 (2019).
48. J. Su, L. Yang, Q. Zhu, H. Wu, Y. He, Y. Liu, J. Xu, D. Jiang, S. Zhang, Active photosynthetic inhibition mediated by MPK3/MPK6 is critical to effector-triggered immunity. *PLoS Biol* **16**, e2004122 (2018).
49. K. D. Pruitt, T. Tatusova, G. R. Brown, D. R. Maglott, NCBI Reference Sequences (RefSeq): current status, new features and genome annotation policy. *Nucleic Acids Res* **40**, D130-135 (2012).
50. S. Deorowicz, A. Debudaj-Grabysz, A. Gudys, FAMSA: Fast and accurate multiple sequence alignment of huge protein families. *Sci Rep* **6**, 33964 (2016).
51. M. N. Price, P. S. Dehal, A. P. Arkin, FastTree 2--approximately maximum-likelihood trees for large alignments. *PLoS One* **5**, e9490 (2010).
52. K. Katoh, D. M. Standley, MAFFT multiple sequence alignment software version 7: improvements in performance and usability. *Mol Biol Evol* **30**, 772-780 (2013).
53. T. L. Bailey, J. Johnson, C. E. Grant, W. S. Noble, The MEME Suite. *Nucleic Acids Res* **43**, W39-49 (2015).
54. S. R. Eddy, Accelerated Profile HMM Searches. *PLoS Comput Biol* **7**, e1002195 (2011).
55. I. Letunic, P. Bork, Interactive Tree Of Life (iTOL) v5: an online tool for phylogenetic tree display and annotation. *Nucleic Acids Res* **49**, W293-W296 (2021).
56. E. Weber, C. Engler, R. Gruetzner, S. Werner, S. Marillonnet, A modular cloning system for standardized assembly of multigene constructs. *PLoS One* **6**, e16765 (2011).
57. C. Engler, M. Youles, R. Gruetzner, T. M. Ehnert, S. Werner, J. D. Jones, N. J. Patron, S. Marillonnet, A golden gate modular cloning toolbox for plants. *ACS Synth Biol* **3**, 839-843 (2014).
58. J. Prautsch, J. L. Erickson, S. Ozyurek, R. Gormanns, L. Franke, Y. Lu, J. Marx, F. Niemeyer, J. E. Parker, J. Stuttmann, M. H. Schattat, Effector XopQ-induced stromule

formation in Nicotiana benthamiana depends on ETI signaling components ADR1 and NRG1. *Plant Physiol* **191**, 161-176 (2023).
59. E. L. H. Yuen, A. Y. Leary, M. Clavel, Y. Tumtas, A. Mohseni, J. Zhao, L. Picchianti, M. Jamshidiha, P. Pandey, C. Duggan, E. Cota, Y. Dagdas, T. O. Bozkurt, A RabGAP negatively regulates plant autophagy and immune trafficking. *Curr Biol* **34**, 2049-2065 e2046 (2024).
60. E. L. H. Yuen, Y. Tumtas, L. I. Chan, T. Ibrahim, E. Evangelisti, F. Tulin, J. Skłenar, F. Menke, S. Kamoun, D. Bubeck, S. Schornack, T. O. Bozkurt, An oomycete effector co-opts a host RabGAP protein to remodel pathogen interface and subvert defense-related secretion. *bioRxiv*, 2024.2001.2011.575225 (2024).
61. H. Wickham, in *ggplot2: Elegant Graphics for Data Analysis,* H. Wickham, Ed. (Springer International Publishing, Cham, 2016), pp. 189-201.
62. P. Pandey, A. Y. Leary, Y. Tumtas, Z. Savage, B. Dagvadorj, C. Duggan, E. L. Yuen, N. Sanguankiattichai, E. Tan, V. Khandare, A. J. Connerton, T. Yunusov, M. Madalinski, F. G. Mirkin, S. Schornack, Y. Dagdas, S. Kamoun, T. O. Bozkurt, An oomycete effector subverts host vesicle trafficking to channel starvation-induced autophagy to the pathogen interface. *Elife* **10**, (2021).
63. V. Gomord, L. A. Denmat, A. C. Fitchette-Laine, B. Satiat-Jeunemaitre, C. Hawes, L. Faye, The C-terminal HDEL sequence is sufficient for retention of secretory proteins in the endoplasmic reticulum (ER) but promotes vacuolar targeting of proteins that escape the ER. *Plant J* **11**, 313-325 (1997).
64. B. K. Nelson, X. Cai, A. Nebenfuhr, A multicolored set of in vivo organelle markers for co-localization studies in Arabidopsis and other plants. *Plant J* **51**, 1126-1136 (2007).
65. Z. Savage, C. Duggan, A. Toufexi, P. Pandey, Y. Liang, M. E. Segretin, L. H. Yuen, D. C. A. Gaboriau, A. Y. Leary, Y. Tumtas, V. Khandare, A. D. Ward, S. W. Botchway, B. C. Bateman, I. Pan, M. Schattat, I. Sparkes, T. O. Bozkurt, Chloroplasts alter their morphology and accumulate at the pathogen interface during infection by Phytophthora infestans. *Plant J* **107**, 1771-1787 (2021).
66. R. H. Kohler, W. R. Zipfel, W. W. Webb, M. R. Hanson, The green fluorescent protein as a marker to visualize plant mitochondria in vivo. *Plant J* **11**, 613-621 (1997).
67. C. Saint-Jore-Dupas, A. Nebenfuhr, A. Boulaflous, M. L. Follet-Gueye, C. Plasson, C. Hawes, A. Driouich, L. Faye, V. Gomord, Plant N-glycan processing enzymes employ different targeting mechanisms for their spatial arrangement along the secretory pathway. *Plant Cell* **18**, 3182-3200 (2006).
68. T. O. Bozkurt, A. Richardson, Y. F. Dagdas, S. Mongrand, S. Kamoun, S. Raffaele, The Plant Membrane-Associated REMORIN1.3 Accumulates in Discrete Perihaustorial Domains and Enhances Susceptibility to Phytophthora infestans. *Plant Physiol* **165**, 1005-1018 (2014).

Supplementary Materials

Materials and Methods

Table S1

Figs. S1 to S10

separately uploaded

Movies S1

Data S1 to S10

Materials and Methods

Phylogenetics and motif analyses

We extracted 110,819 NLR (Nucleotide-binding Leucine-rich Repeat) proteins from the NLRtracker outputs of 178 RefSeq plant proteomes (*49*), available on Zenodo (Data S1) [10.5281/zenodo.13627395]. From these, 98,733 NLRs were identified based on specific domain architectures: "CNL", "CNLO", "CN", "OCNL", "CONL", "NL", "NLO", "ONL", "BCNL", "BNL", "BCN", "BCCNL", "BNLO", "BOCNL", "RNL", "TN", "TNL", "TNLO", and "TNLJ". To reduce redundancy, we deduplicated the dataset, retaining 63,125 unique NLR sequences. Further refinement involved filtering the sequences based on NB-ARC domain length, specifically retaining those between 250 and 400 amino acids. This step resulted in 56,280 NLRs for downstream analysis (Data S2). These NB-ARC domain sequences were aligned to the RefPlantNLR database using FAMSA v2.2.2 (*10, 50*), followed by phylogenetic tree construction using FastTree 2 v2.1.10 with the LG model (*51*). From the resulting tree, we identified and extracted an RPW8-NLR clade comprising 1,140 sequences based on the inclusion of known reference ADR1 and NRG1 sequences (Data S2). A new NB-ARC tree was generated for these RPW8-like (CC_R) NLRs using MAFFT v7.525 with the [--anysymbol] option for alignment and FastTree 2 with the LG model. AtZAR1, NbZAR1, SlNRC0, SlNRC1, SlNRC2, SlNRC3, SlNRC4a, SlNRC4b, and SlNRC6 sequences were used as outgroups (*52*). To identify conserved motifs within the RPW8-like CC domains of these sequences, we extracted the domain sequences from the first residue to the start of the NB-ARC domain, excluding those shorter than 100 amino acids to avoid truncated sequences. MEME v5.5.1 [-maxw 30 -nmotifs 5 -mod zoops] was used to detect conserved motifs in the RPW8 domains of the ADR1 and NRG1 clades (Data S3, S4) (*53*). The N-terminal motifs identified by MEME were then used to create Hidden Markov Models (HMMs) using the hmmbuild software from the HMMER suite (Data S5, S6). These HMMs were searched against the initial NLR datasets using hmmsearch with the [--max] option. As a control, the MADA N-terminal motif was included to assess the distribution of N-terminal motifs (*30, 54*). Hits with e-values of 0.05 or lower were retained and mapped onto the initial NLR phylogenetics tree. The resulting trees were visualized using iTOL (*55*). All scripts used in this analysis are available on https://github.com/amiralito/NRG1_Localization.

Structural analyses (AlphaFold3)

The AlphaFold3 web server (https://golgi.sandbox.google.com/) was used to model pentamers for AtZAR1, TmSr35, NbADR1 and NbNRG1, and hexamer for NbNRC2 with 50 oleic acids as a proxy for the plasma membrane (*29*). AtZAR1 and TmSr35 were modeled as pentamers and NbNRC2 as an hexamer based on their cryoEM structures (PDB ID:6J5T (*7*), 7XC2 (*15*) and 9FP6 (*19*), respectively). The default seed was set to 1. From each modeling run, only the top-ranked model (model_0) was retained and processed (Data S7). The ipTM and pTM values were extracted from the AlphaFold3 JSON files using custom scripts. PAE plots for models were downloaded from the AlphaFold3 web server.

Molecular cloning

We employed the Golden Gate Modular Cloning (MoClo) kit (*56*) along with the MoClo Plant Parts kit (*57*) for cloning purposes. Unless otherwise specified, all vectors were constructed using these kits. Cloning design and sequence analysis were performed using Geneious Prime (v2023.2.1; www.geneious.com). Detailed information on plasmid construction can be found in Table S1.

Plant material

Wildtype and transgenic *N. benthamiana* plants were grown in a regulated growth chamber set at 24°C. The transgenic *nrg1/adr1* double KO plants were obtained from the Schattat lab (*58*). To generate *nrg1* KO plants, the following primer pairs were used to manufacture guide RNA sequences targeting *nrg1*: CAGTATTCGATGACATCGAG(AGG) and GCTTGAGGAGAAAGAGAAGG(TGG). The primers used for genotyping *nrg1* KO plants were GAGCTGCTCTTGGTCCAGTT and TTGATATCATCCTCTTGACAAAGC (Data S9). The cultivation medium of the plants consisted of a blend of organic soil, mixed in a 3:1 ratio of Levington's F2 soil with sand and Sinclair's 2-5 mm vermiculite. The plants were exposed to intense light and maintained under long-day conditions, with a photoperiod of 16 hours of light and 8 hours of darkness. The experiments were conducted on plants aged between 4 and 5 weeks.

Confocal laser scanning microscopy

Confocal microscopy was performed 2-3 days post-agroinfiltration as described previously (*59, 60*). Leaf tissue samples were collected using a size 4 cork borer, submerged in dH2O, and mounted live on glass slides for imaging. The abaxial side of the leaf tissue was imaged using a Leica STELLARIS 5 inverted confocal microscope with a 63x water immersion objective lens. The emission wavelengths for GFP and RFP tags were set to 495-550 nm and 570-620 nm, respectively. The confocal images were analyzed using ImageJ.

Agrobacterium-mediated transient gene expression in *N. benthamiana*

Agrobacterium-mediated transient gene expression was carried out via agroinfiltration as described previously (*59*). The *Agrobacterium tumefaciens* strain containing the target plasmid was first rinsed with water and then resuspended in an agroinfiltration buffer composed of 10 mM MES and 10 mM MgCl2 (pH 5.7). The OD_{600} of the bacterial suspension was measured and then adjusted according to the specific construct and experimental requirements. Finally, the prepared bacterial suspension was infiltrated into 4 to 5-week-old *N. benthamiana* leaves using a 1 ml Plastipak syringe without a needle.

Cell death assay

Cell death elicitors were introduced into the abaxial side of *N. benthamiana* leaves via agroinfiltration. At 3 dpi, the leaves were detached and subjected to both daylight and infrared imaging. Infrared imaging was performed using the 800 nm channel of the LI-COR Odyssey Fc Imager. The resulting infrared images were analyzed with the "Analysis" function in LI-COR Image Studio. The HR signal was determined by dividing the signal intensity of the cell

death spot by its area and then normalizing the value on a scale of up to 10 points. The normalized HR signal was plotted using ggplot in R (*61*). Raw and normalized HR intensity data can be found at Data S10.

Image processing and data analysis

Confocal microscopy images were processed using Leica LAS X software and ImageJ. Image analysis and quantification for cell death experiments were conducted with LI-COR Image Studio. Data were represented using box-and-dot plots created with ggplot2 in R (*61*).

Table S1. List of all constructs used in this research

Construct	Plasmids	Reference
35S::NRG1:GFP (with P19)	pJK268c_mRFP1, pICH51288, pJK-0-320, pICSL50034, pICH41414	This work
35S::NRG1:GFP (without P19)	pJK001c_mRFP1, pICH51288, pJK-0-320, pICSL50034, pICH41414	This work
35S::NRG1:mKOK (without P19)	pJK001c_mRFP1, pICH51288, pJK-0-320, pICH41414	This work
35S::NRG1$^{\Delta 14}$:GFP (with P19)	pJK268c_mRFP1, pICH51288, pJK-0-321, pICSL50034, pICH41414	This work
35S::NRG1$^{\Delta 14}$:GFP (without P19)	pJK001c_mRFP1, pICH51288, pJK-0-321, pICSL50034, pICH41414	This work
35S::EV:GFP (with P19)	pJK268c_mRFP1, pICH51288, pICSL50034, pICH41414	This work
35S::EV:GFP (without P19)	pJK001c_mRFP1, pICH51288, pICSL50034, pICH41414	This work
p*At*Act2::NRG1$^{\Delta 14}$:GFP (without P19)	pJK001c_mRFP1, pICH87644, pJK-0-321, pICSL50034, pICH41414	This work
35S::ADR1:GFP (with P19)	pJK268c_mRFP1, pICH51288, pJK-0-318, pICSL50034, pICH41414	This work
35S::ADR1$^{\Delta 14}$:GFP (with P19)	pJK268c_mRFP1, pICH51288, pFK0A-0164, pICSL50034, pICH41414	This work
35S::ADR1$^{\Delta 14}$:GFP (without P19)	pJK001c_mRFP1, pICH51288, pFK0A-0164, pICSL50034, pICH41414	This work
CC$^{ADR1\Delta 14}$-NRG1:GFP (with P19)	pJK268c_mRFP1, pICH51288, pFK0A-	This work

	0165, pICSL50034, pICH41414	
$CC^{NRG1\Delta14}$-ADR1:GFP (with P19)	pJK268c_mRFP1, pICH51288, pFK0A-0166, pICSL50034, pICH41414	This work
pl2m-2x35s::XopQ	pJK001c_mRFP1, pICH51288, pUC57-Kan-XopQ, pICH41414	This work
$NRC4^{L9E/DV}$:GFP	/	(*24*)
FLAG:GUS	/	(*62*)
RFP:EV	/	(*60*)
RFP:ER (SP:RFP:HDEL)	/	(*63-65*)
Mitochondria:mCherry ($ScCOX4_{1-29}$:mCherry)	/	(*62, 64, 66*)
CTP1:mCherry	/	(*35*)
Golgi:mCherry ($GmMan1_{1-49}$:mCherry)	/	(*62, 64, 67*)
RFP:Remorin1.3	/	(*68*)

Supplemental Figures

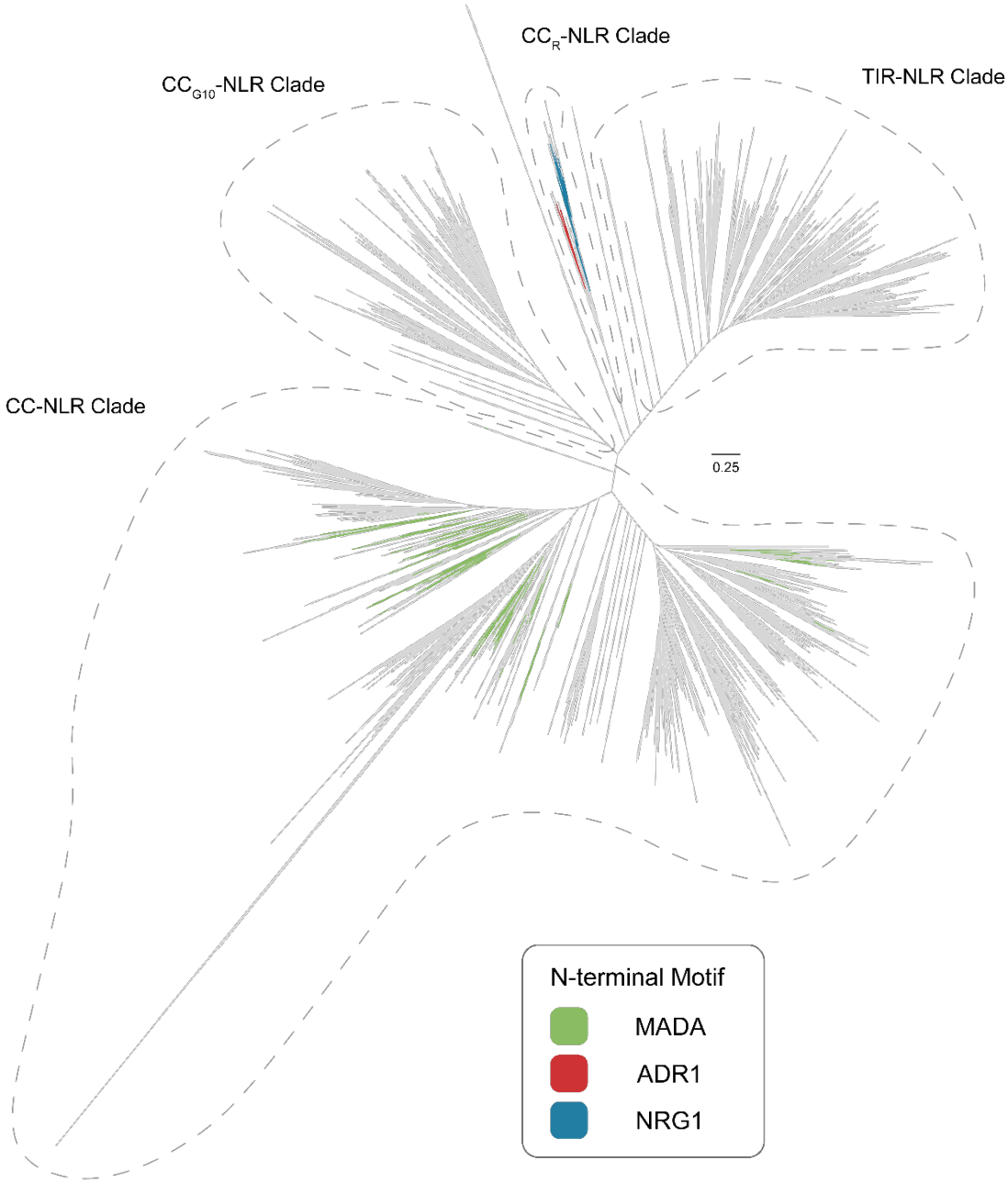

Fig. S1. Phylogenetic tree of 56,280 NLRs from 178 RefSeq reference plant proteomes. The ADR1 and NRG1 N-terminal motifs are confined to their respective sub-clades within the RPW8 (CC_R)-NLR clade, while the MADA N-terminal motif exhibits a broader distribution across the CC-NLR clade. N-terminal motifs discovered using MEME analysis were used to make HMM profiles and searched against the 56,280 NLRs (Data S5, S6).

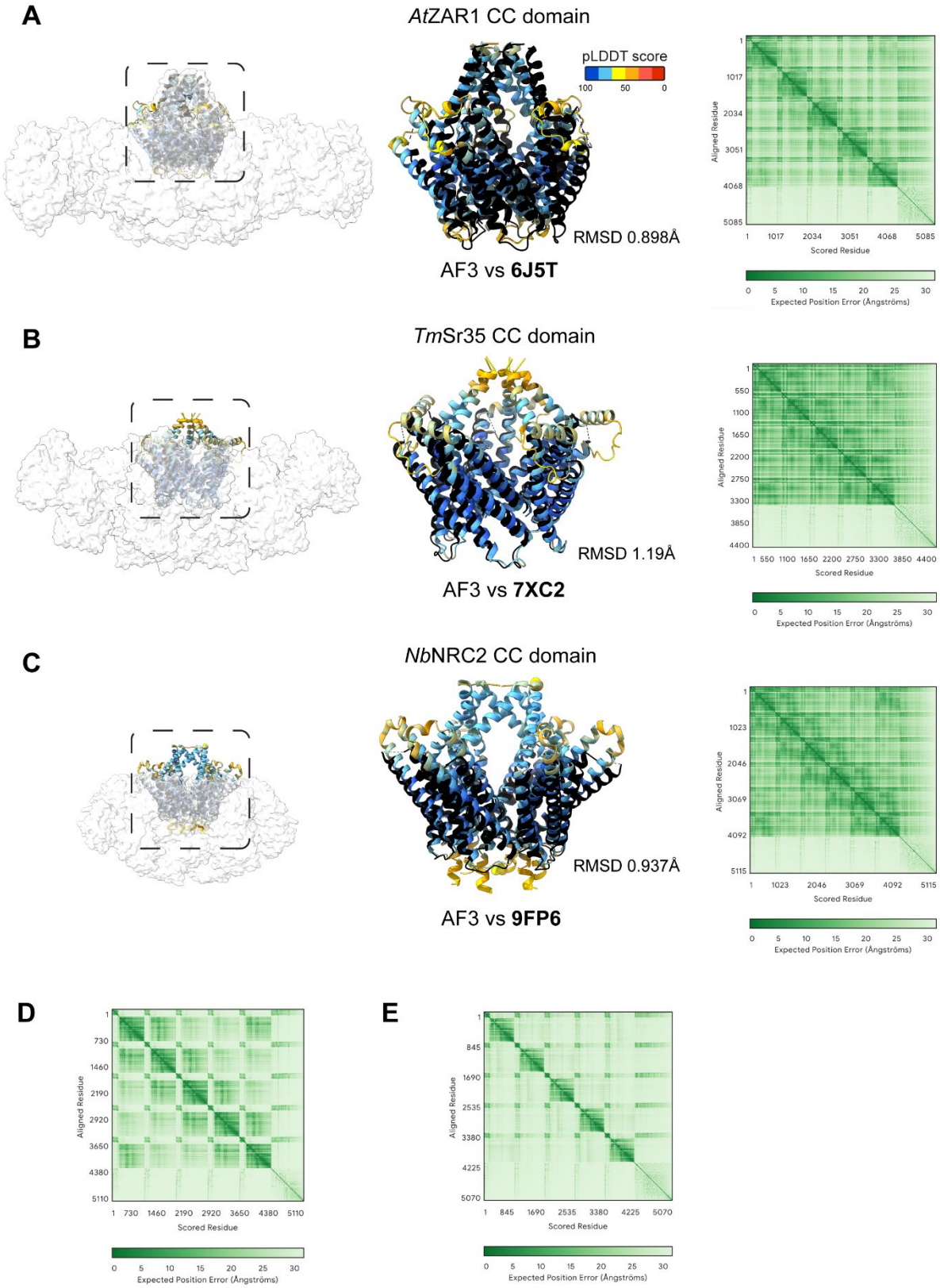
A
AtZAR1 CC domain
pLDDT score
100 50 0
RMSD 0.898Å
AF3 vs 6J5T
Aligned Residue
Scored Residue
Expected Position Error (Ångströms)
B
TmSr35 CC domain
RMSD 1.19Å
AF3 vs 7XC2
Aligned Residue
Scored Residue
Expected Position Error (Ångströms)
C
NbNRC2 CC domain
RMSD 0.937Å
AF3 vs 9FP6
Aligned Residue
Scored Residue
Expected Position Error (Ångströms)
D
Aligned Residue
Scored Residue
Expected Position Error (Ångströms)
E
Aligned Residue
Scored Residue
Expected Position Error (Ångströms)

Fig. S2. Quality analysis of AlphaFold3 predicted resistosome and coiled-coil domain structures. (A) Coiled-coil domain structure (black) and AlphaFold3 prediction (coloured by pLDDT) overlaid and fitted into the cryoEM density map of AtZAR1 (6J5T) with an RMSD of 0.898Å.The PAE plot for AlphaFold3 prediction of AtZAR1 resistosome was downloaded from the AlphaFold3 server. **(B)** Coiled-coil domain structure (black) and AlphaFold3 prediction (coloured by pLDDT) overlaid and fitted into the cryoEM density map of TmSr35 (7XC2) with an RMSD of 1.19Å.The PAE plot for AlphaFold3 prediction of TmSr35 resistosome was downloaded from the AlphaFold3 server. **(C)** Coiled-coil domain structure (black) and AlphaFold3 prediction (coloured by pLDDT) overlaid and fitted into the cryoEM density map of NbNRC2 (9FP6) with an RMSD of 0.937Å.The PAE plot for AlphaFold3 prediction of NbNRC2 resistosome was downloaded from the AlphaFold3 server. **(D)** The PAE plot for AlphaFold3 prediction of NbNRG1 resistosome was downloaded from the AlphaFold3 server. **(E)** The PAE plot for AlphaFold3 prediction of NbADR1 resistosome was downloaded from the AlphaFold3 server. AlphaFold3 models for studied resistosomes can be found at Data S7.

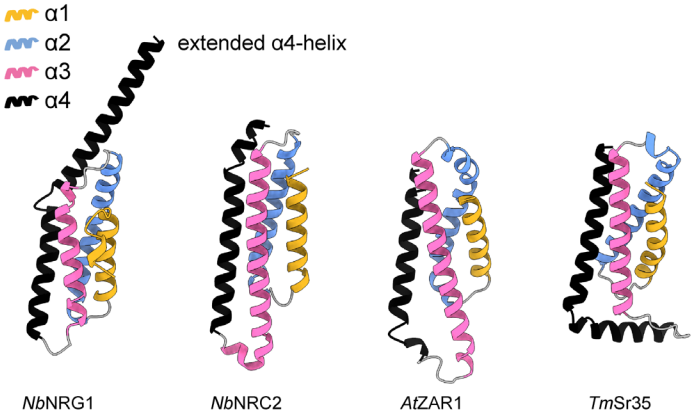

Fig. S3. CC_R-NLR NbNRG1 has an extended fourth alpha-helix in the coiled-coil domain compared to CC-NLRs NbNRC2, AtZAR1 and TmSr35. Alpha-helix one is coloured yellow, two blue, three pink and four black in all presented models.

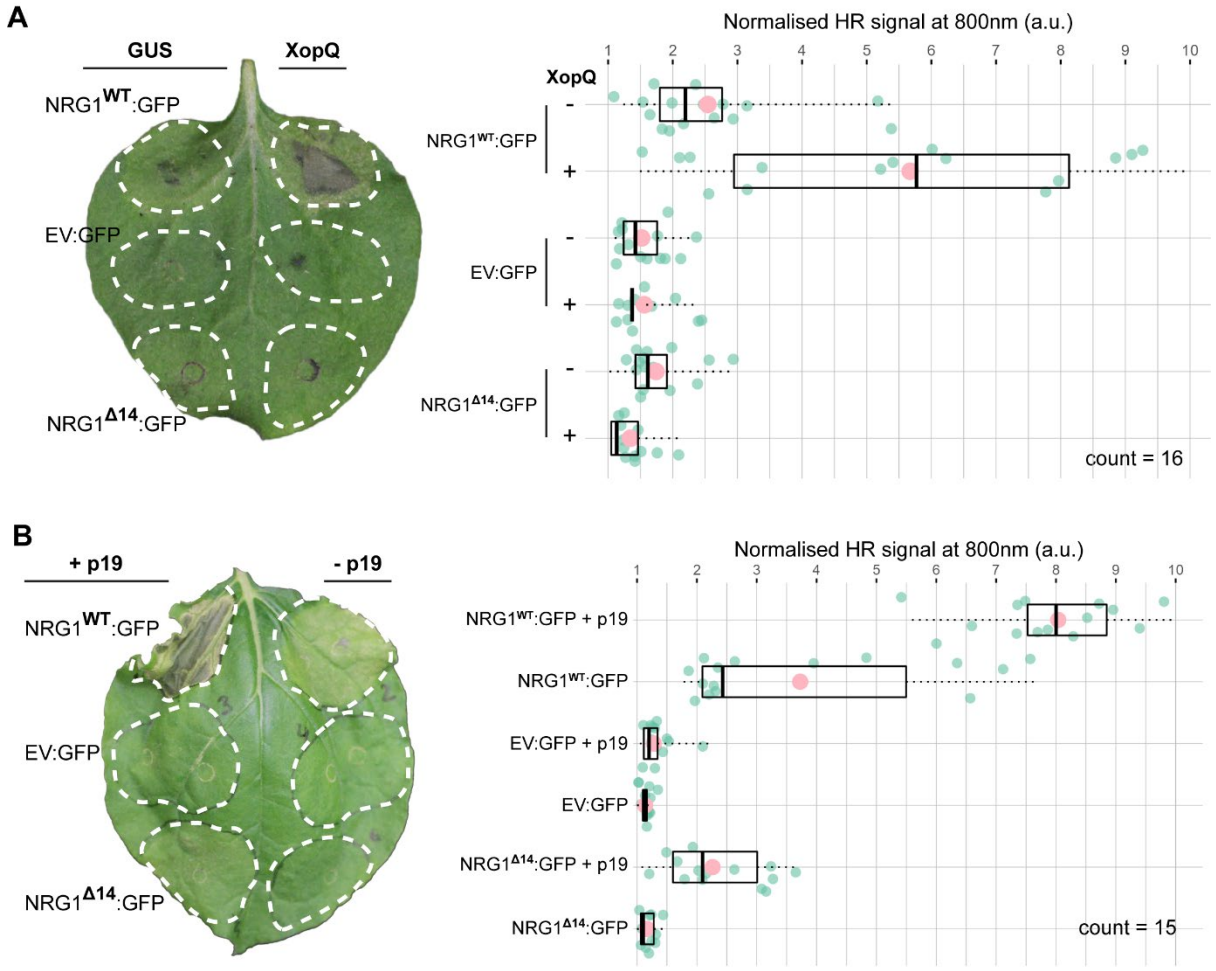

Fig. S4. NbNRG1-dependent HR can be amplified by XopQ and P19. (A) A representative leaf picture from *N. benthamiana nrg1* KO plants showing HR after expression of NRG1:GFP, NRG1$^{\Delta 14}$:GFP or EV:GFP with GUS control or XopQ. Box and dot plot showing the normalized HR signal at 800 nm (infrared) for 16 leaves. Each leaf is highlighted with a green dot and the mean value for that condition in a larger pink dot. **(B)** A representative leaf picture from *N. benthamiana nrg1* KO plants showing HR after expression of NRG1:GFP, NRG1$^{\Delta 14}$:GFP or EV:GFP with and without P19. Box and dot plot showing the normalized HR signal at 800 nm (infrared) for 15 leaves. Each leaf is highlighted with a green dot and the mean value for that condition in a larger pink dot.

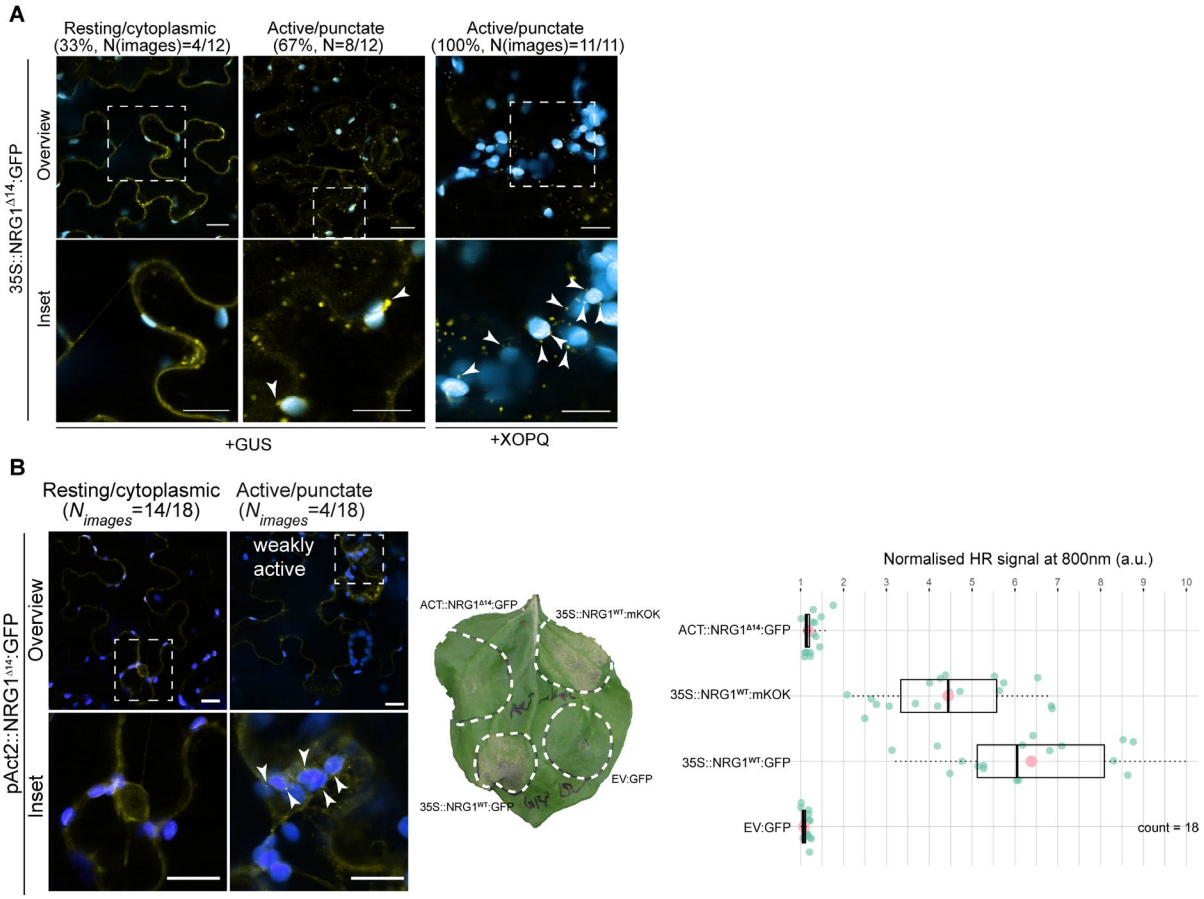

Fig. S5. NbNRG1$^{\Delta 14}$ behaves like NbNRG1 in localizing to the chloroplast outer envelope. **(A)** Confocal micrographs of *N. benthamiana* leaf epidermal cells transiently expressing 35S::NRG1$^{\Delta 14}$:GFP with XopQ or GUS control. Images shown are single-plane images. Dashed lines in overview correspond to inset. Arrows indicate examples of puncta around chloroplasts. Scale bars represent 10 µm. **(B)** Confocal micrographs of *N. benthamiana* leaf epidermal cells transiently expressing pAct2::NRG1$^{\Delta 14}$:GFP with XopQ or GUS control. Images shown are single-plane images. Dashed lines in overview correspond to inset. Arrows indicate examples of puncta around chloroplasts. Scale bars represent 10 µm. A representative leaf picture from *N. benthamiana* nrg1 KO plants showing HR after expression of pAct2:NRG1$^{\Delta 14}$:GFP, 35S:NRG1$^{\Delta 14}$:GFP, or 35S:NRG1:mKOK. Box and dot plot showing the normalized HR signal at 800 nm (infrared) for 18 leaves. Each leaf is highlighted with a green dot and the mean value for that condition in a larger pink dot.

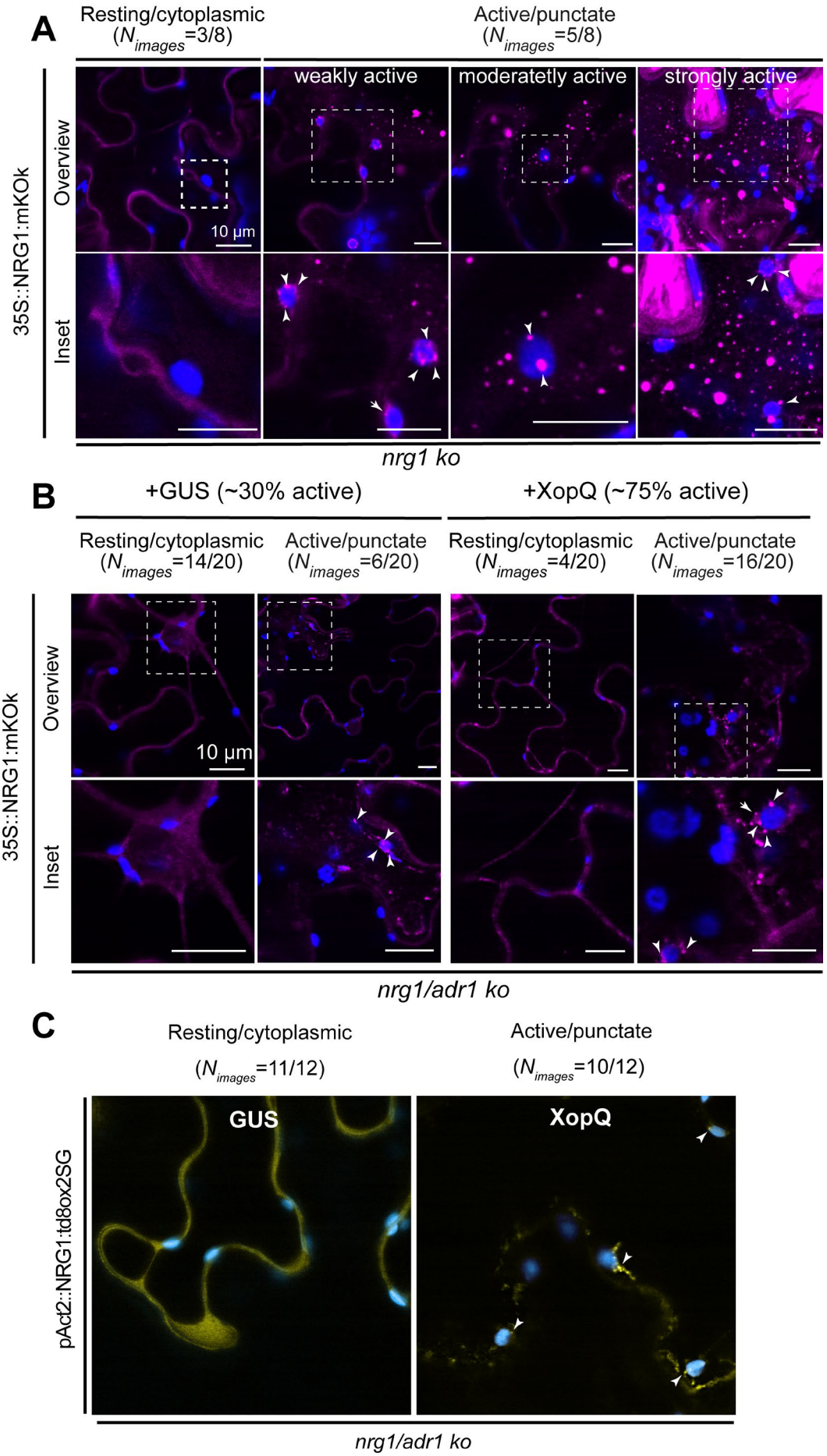
A
Resting/cytoplasmic
(N_{images}=3/8)
Active/punctate
(N_{images}=5/8)
weakly active
moderatetly active
strongly active
35S::NRG1:mKOk
Overview
Inset
10 µm
nrg1 ko
B
+GUS (~30% active)
+XopQ (~75% active)
Resting/cytoplasmic
(N_{images}=14/20)
Active/punctate
(N_{images}=6/20)
Resting/cytoplasmic
(N_{images}=4/20)
Active/punctate
(N_{images}=16/20)
35S::NRG1:mKOk
Overview
Inset
10 µm
nrg1/adr1 ko
C
Resting/cytoplasmic
(N_{images}=11/12)
Active/punctate
(N_{images}=10/12)
GUS
XopQ
pAct2::NRG1:td8ox2SG
nrg1/adr1 ko

Fig. S6. Alternative fluorescent constructs produced weaker cell death allowing resting state imaging of full-length NbNRG1. (A) Confocal micrographs of *N. benthamiana nrg1* KO leaf epidermal cells transiently expressing 35S::NRG1:mKOK. Images shown are single-plane images. Dashed lines in overview correspond to inset. Arrows indicate examples of puncta around chloroplasts. Scale bars represent 10 µm. **(B)** Confocal micrographs of *N. benthamiana nrg1/adr1* double KO leaf epidermal cells transiently expressing 35S::NRG1:mKOK with XopQ or GUS control. Images shown are single-plane images. Dashed lines in overview correspond to inset. Arrows indicate examples of puncta around chloroplasts. Scale bars represent 10 µm. **(C)** Confocal micrographs of *N. benthamiana* leaf epidermal cells transiently expressing pAct2::NRG1:td8ox2SG with XopQ or GUS control. Images shown are single-plane images. Scale bar represents 10 µm.

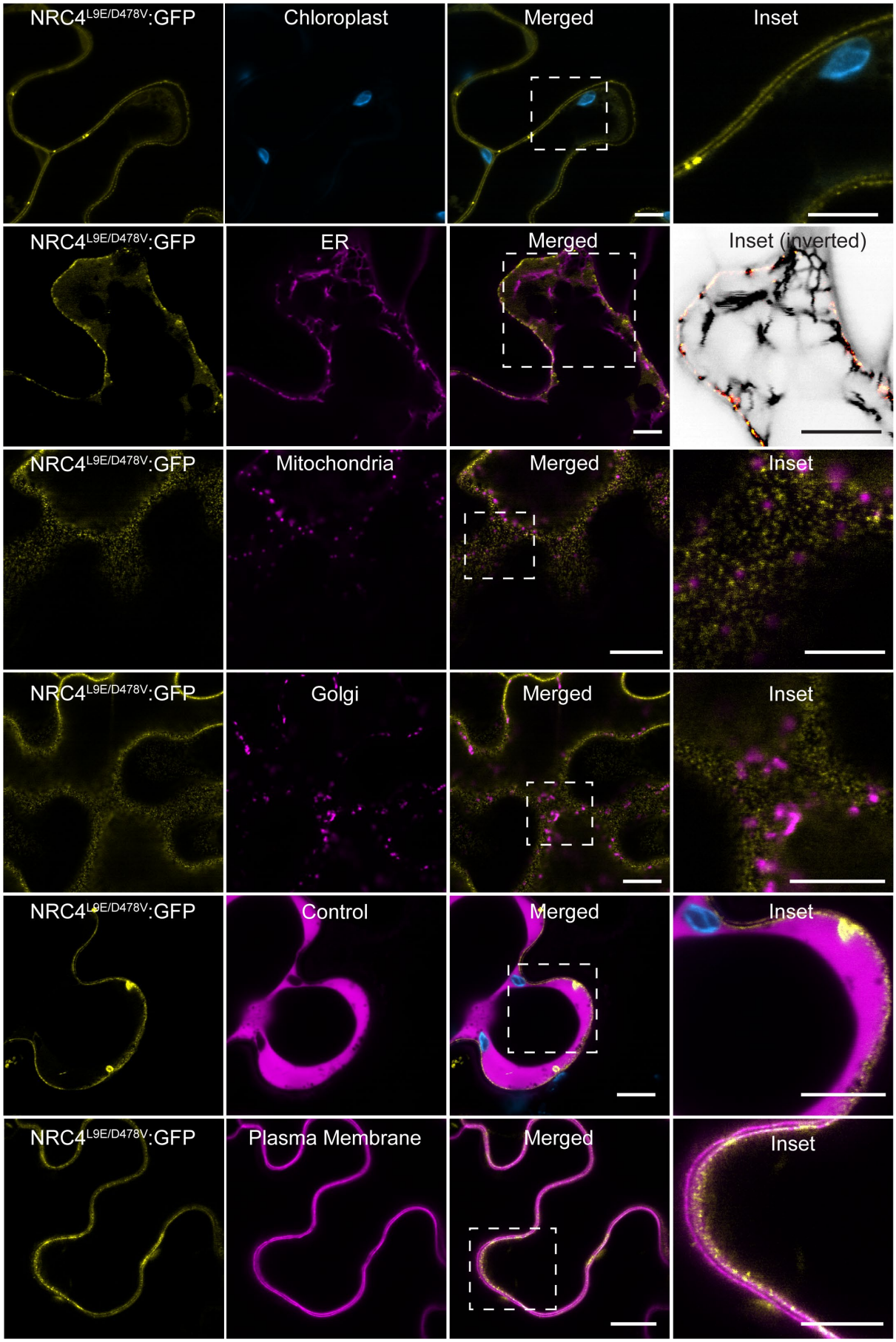
NRC4L9E/D478V:GFP
Chloroplast
Merged
Inset
NRC4L9E/D478V:GFP
ER
Merged
Inset (inverted)
NRC4L9E/D478V:GFP
Mitochondria
Merged
Inset
NRC4L9E/D478V:GFP
Golgi
Merged
Inset
NRC4L9E/D478V:GFP
Control
Merged
Inset
NRC4L9E/D478V:GFP
Plasma Membrane
Merged
Inset

Fig. S7. Autoactive CC-NLR NbNRC4 does not localize to organellar membranes. Confocal micrographs of *N. benthamiana* leaf epidermal cells transiently expressing NRC4$^{L9E/D478V}$:GFP with SP:RFP:HDEL (ER), CTP1-RFP (mitochondria), GmMan11-49:mCherry (Golgi), RFP-Remorin1.3 (plasma membrane) or RFP:EV (control). Chloroplasts were visualized through autofluorescence. Images shown are single-plane images. Dashed lines in the merged panel correspond to inset. Arrows indicate examples of puncta around chloroplasts. Scale bars represent 10 µm.

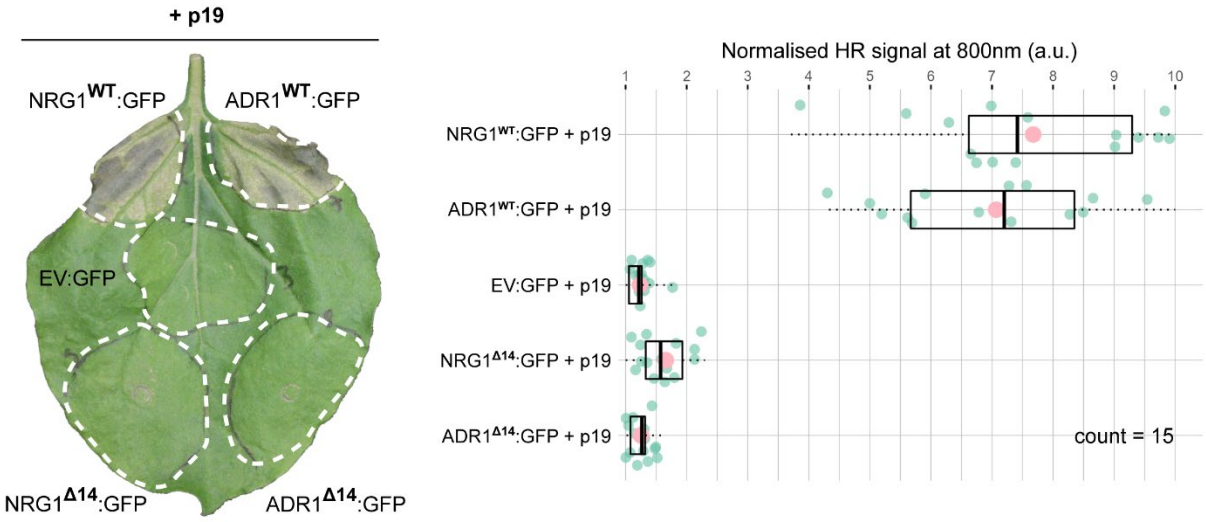

Fig. S8. Similar to NbNRG1, deletion of the first 14 amino acids of NbADR1 attenuates HR symptoms. A representative leaf picture from *N. benthamiana nrg1* KO plants showing HR after expression of NRG1:GFP, NRG1$^{\Delta 14}$:GFP, ADR1:GFP, ADR1$^{\Delta 14}$:GFP or EV:GFP with P19. Box and dot plot showing the normalized HR signal at 800 nm (infrared) for 15 leaves. Each leaf is highlighted with a green dot and the mean value for that condition in a larger pink dot.

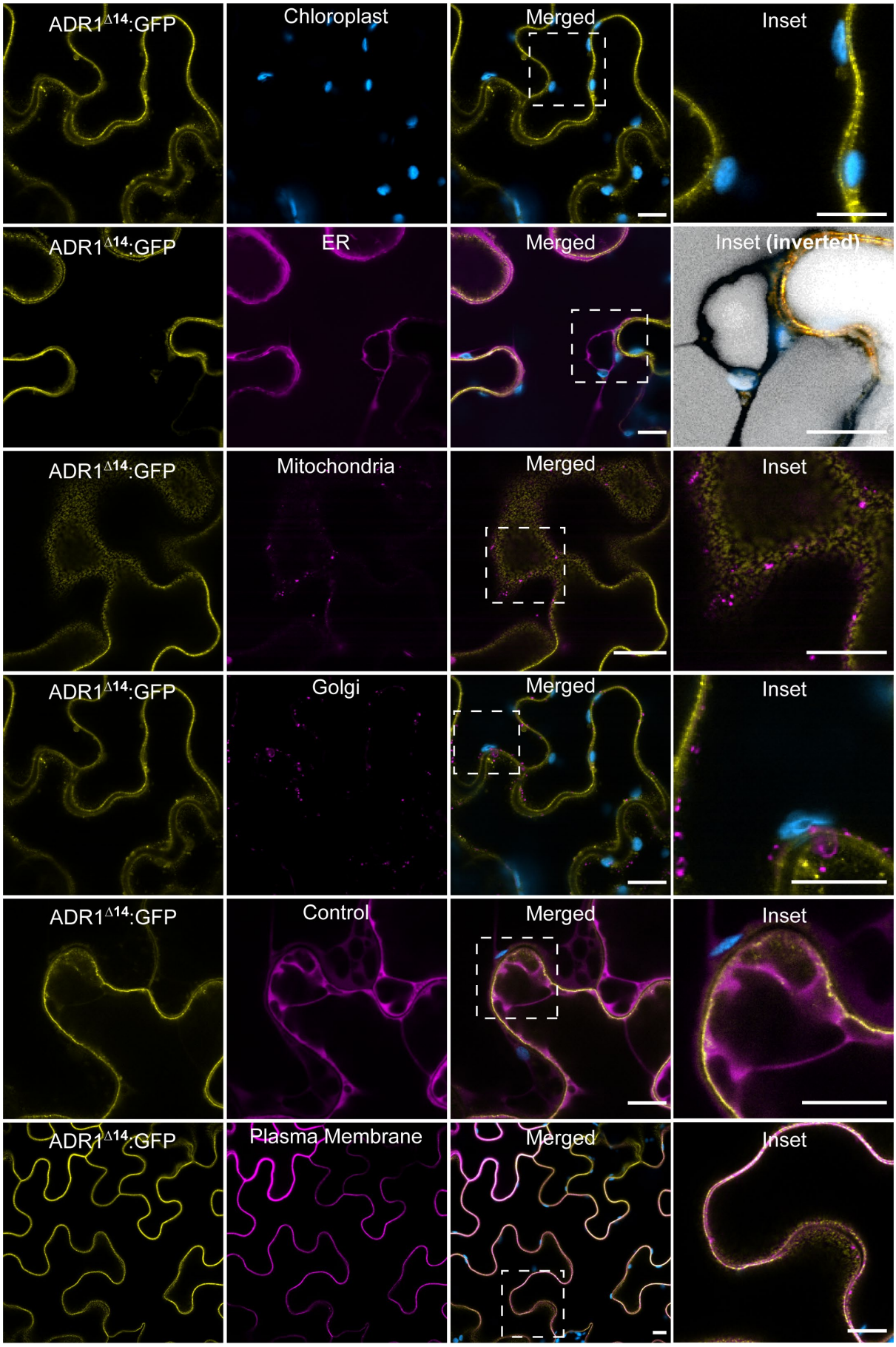
ADR1Δ14:GFP
Chloroplast
Merged
Inset
ADR1Δ14:GFP
ER
Merged
Inset (inverted)
ADR1Δ14:GFP
Mitochondria
Merged
Inset
ADR1Δ14:GFP
Golgi
Merged
Inset
ADR1Δ14:GFP
Control
Merged
Inset
ADR1Δ14:GFP
Plasma Membrane
Merged
Inset

Fig. S9. CC_R-NLR NbADR1 targets the plasma membrane and not organelle membranes. Confocal micrographs of *N. benthamiana* leaf epidermal cells transiently expressing $ADR1^{\Delta 14}$:GFP with SP:RFP:HDEL (ER), CTP1:RFP (mitochondria), GmMan11-49:mCherry (Golgi), RFP:Remorin1.3 (plasma membrane) or RFP:EV (control). Chloroplasts were visualized through autofluorescence. Images shown are single-plane images. Dashed lines in the merged panel correspond to inset. Scale bars represent 10 µm.

N. benthamiana epss KO

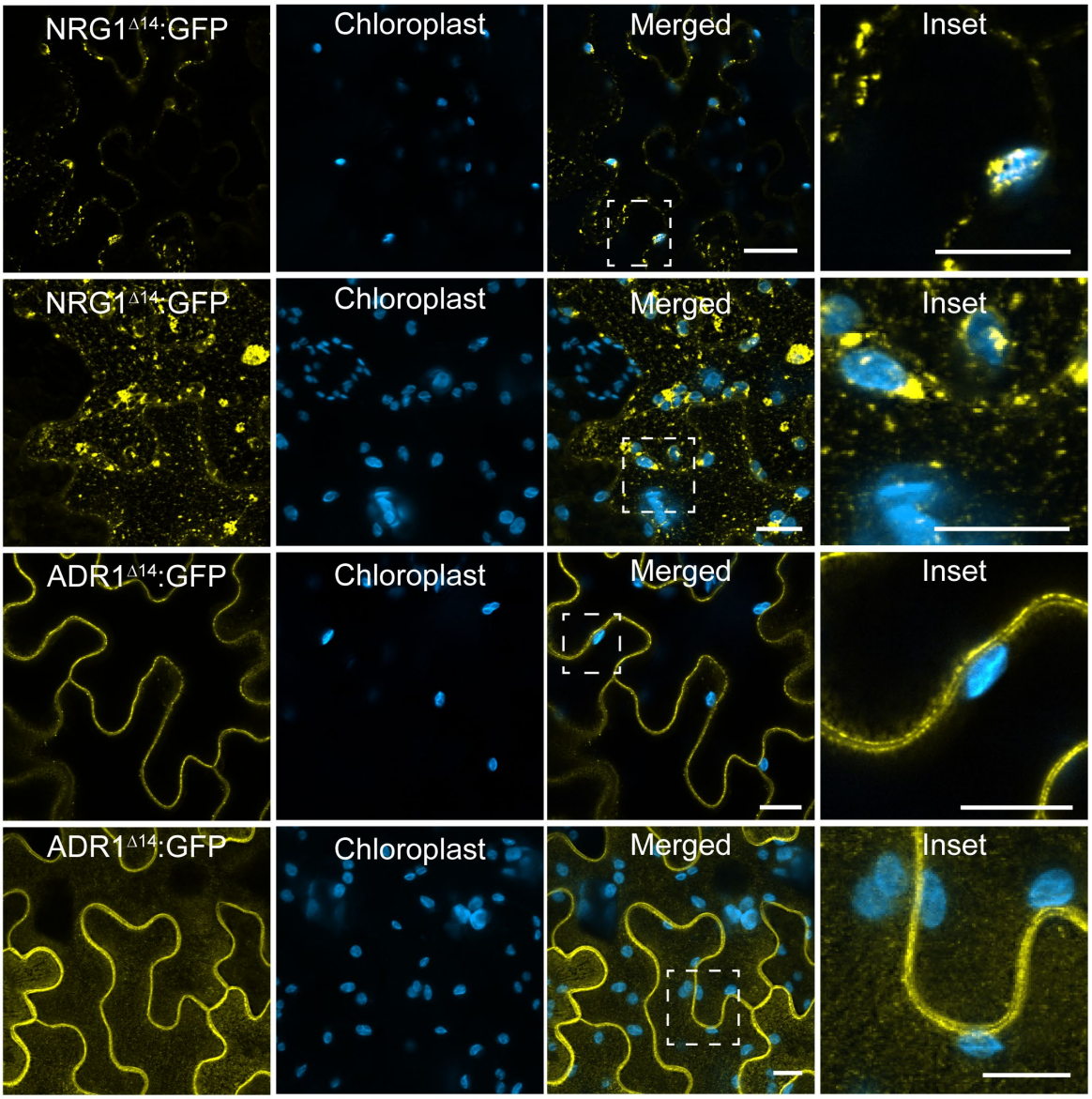

wildtype *N. benthamiana*

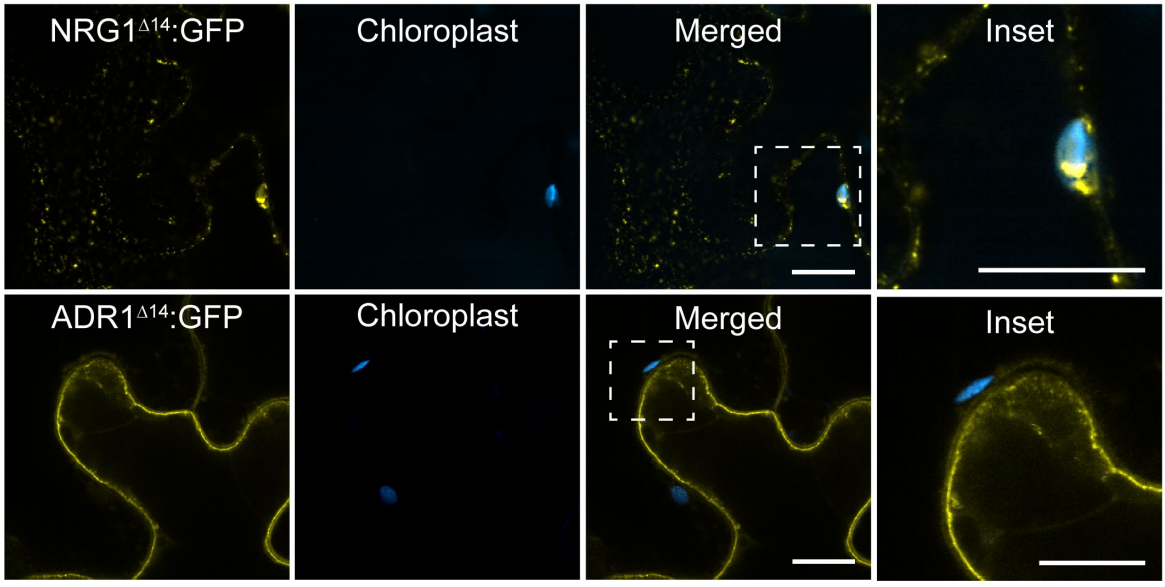

Fig. S10. Localization patterns of CC_R-NLRs NbNRG1 and NbADR1 are independent of EDS1-mediated signaling. Top panel: confocal micrographs of *N. benthamiana epss* KO leaf epidermal cells transiently expressing $NRG1^{\Delta 14}$:GFP and $ADR1^{\Delta 14}$:GFP. Chloroplasts were visualized through autofluorescence. Panels 1 and 3 are single plane images. Panel 2 and 4 are maximal projections of 25 frames with 1 µm steps and 15 frames with 1 µm steps, respectively. Dashed lines in the merged panel correspond to inset. Scale bars represent 10 µm. Bottom panel: confocal micrographs of wild-type *N. benthamiana* leaf epidermal cells transiently expressing $NRG1^{\Delta 14}$:GFP and $ADR1^{\Delta 14}$:GFP. Chloroplasts were visualized through autofluorescence. Images shown are single-plane images. Dashed lines in the merged panel correspond to inset. Scale bars represent 10 µm.